McClelland Lecture
Analytical contributions to offshore geotechnical engineering

Conférence McClelland
Contributions des méthodes analytiques à la géotechnique offshore

Randolph M. F.
Centre for Offshore Foundation Systems, University of Western Australia

ABSTRACT: The theme of this paper, the written version of the 2nd McClelland Lecture, is the contribution of analysis to offshore geotechnical engineering. The application areas considered range from the axial and lateral response of piles, to seabed infrastructure associated with deep water applications, including shallow skirted foundations, anchors, pipelines and risers. The emphasis throughout is on analytical solutions, including appropriately framed outcomes of numerical studies. Most of the material is retrospective, summarising key contributions in an effort to facilitate access, and thus help close the gap between theory and practice.

RÉSUMÉ : L'objet de cet article, la 2e conférence McClelland, est de présenter les contributions des méthodes analytiques à la géotechnique offshore. Il couvre plusieurs champs d'application, de la capacité axiale et horizontale des pieux au comportement des structures géotechniques associées aux développements en eaux profondes, incluant notamment les fondations superficielles avec jupe, les systèmes d'ancrages et les pipelines. L'accent est notamment porté sur les solutions analytiques, dont certaines sont basées sur des résultats de solutions numériques. L'essentiel du contenu de cet article résume les contributions antérieures les plus significatives, de façon à en faciliter l'accès et ainsi réduire l'écart entre théorie et pratique.

KEYWORDS: Analysis, consolidation, offshore engineering, penetrometers, pile foundations, pipelines, shallow foundations.

1 INTRODUCTION

I was privileged to meet Bram McClelland on a few occasions and have always held him in the highest regard. Much of my early exposure to the offshore world was through interactions with the London and Houston branches of the consulting company, McClelland Engineers, that he founded. It was therefore a great honour to be invited to give this, the 2nd, McClelland Lecture, and I am gratified that the written version of the lecture is to form part of the proceedings of the 18th International Conference on Soil Mechanics and Geotechnical Engineering. Following in the footsteps of the first McClelland Lecturer, Don Murff (Murff, 2012), is no easy feat, although I must admit to having become somewhat accustomed to this during my career. More times than I can remember I have found (often retrospectively) that an analytical contribution I have offered has been covered elegantly by Don in a prior publication. It is fitting, therefore, to continue the theme of his own McClelland lecture, in targeting the gap between theory and practice, drawing attention to and summarising various analytical contributions.

In an era where virtually any geotechnical application can be modelled numerically, with idealisations potentially limited only to those associated with the constitutive response of the soil, it is tempting to wonder whether true analytical solutions still have a role. At the opposite extreme, design guidelines such as API (2011) and ISO (2003, 2007) are inevitably slow to evolve and in many places rely on somewhat dated suggestions, either empirical or quasi-analytical. There is limited incentive to refine them through analysis without clear evidence of lack of conservatism, or the reverse, excessive conservatism.

The potential of analysis is its ability to provide a direct, ideally quantitative, link between a required output and the various input parameters for a given application. At a basic level, dimensional analysis should indicate appropriate non-dimensional forms for input and output quantities. Analytical solutions will typically contain idealisations, either of the problem geometry or of the soil response, for example linear elasticity for stiffness solutions, or perfect plasticity for capacity solutions. However, they still provide a framework linking the outcome to the various input parameters, highlighting the critical sensitivities of the response, facilitating parametric studies and quantifying the effect of different idealisations.

The paper takes a retrospective look at some of the analytical contributions relevant to offshore geotechnical engineering, drawing attention to the potential application of the solutions in design guidelines and day to day practice. The first part of the paper revisits solutions for the axial and lateral response of pile foundations, which are still the main type of foundation for offshore structures in moderate or shallow water depths and for tension leg platforms in deeper water. The remainder of the paper then focuses more on applications relevant for deep water developments, including subsea foundations, anchors and pipelines. Of necessity, restrictions on the length of the paper have required me to focus on a few specific issues within each topic, in particular where solutions point the way towards improved design recommendations, and recent work addressing developing areas of offshore geotechnical engineering.

Before discussing the applications themselves, I should clarify what I intend by the word 'analytical' within the present context. I include within this term appropriately conceived parametric studies undertaken through numerical analysis. These should lead to algebraic expressions or charts that may be used in design, identifying the relative contribution of non-dimensional groups of parameters that affect the result. By contrast, an algebraic fit through experimental data will rarely provide comparable insight, and should instead be taken as encouragement to quantify the phenomenon through analytical or numerical means. That said, I have always been a strong proponent of the need for high quality experimental data, but with the primary objectives of stimulating understanding of the problem for subsequent analysis, and where necessary to calibrate specific areas of uncertainty in analytical models.

2 PILE FOUNDATIONS

2.1 *Axial shaft friction*

Arguably the most important aspect of pile design, estimation of the profile of limiting shaft friction, has proved resistant to analytical treatment, although understanding of the processes involved has gradually developed. This has allowed appropriate non-dimensional quantities on which the limiting shaft friction depends to be identified. A full discussion of the current design recommendations for shaft friction was provided recently by Jeanjean (2012), and so the remarks below are limited to relatively high level principles underlying the guidelines.

In clays and other fine-grained soils, where installation of driven piles occurs over a shorter time scale than dissipation of excess pore pressures, the main quantities to be considered are the undrained shear strength, s_u, of the sediments, the vertical effective stress, σ'_{v0}, and pile geometry: diameter, D, and embedment length, L. It may also be necessary to consider the distance, h, of the element in question from the pile tip. With these parameters as input, empirical correlations have then been used to establish guidelines for the limiting shaft friction, τ_f, normalised by s_u or σ'_{v0}, as a function of s_u/σ'_{v0}, L/D and h/D. Other quantities such as the internal angle of friction, and in situ stress ratio, K_0, are captured to some extent by the strength ratio, s_u/σ'_{v0}, at least within the accuracy of the empirical database. In some clays it may also be necessary to consider the extent to which shaft friction may be limited by a low interface friction angle between pile and soil, or immediately adjacent to the pile, due to the formation of residual surfaces in the clay.

For sands, the cone resistance, q_c (more strictly the net resistance, q_{net}) essentially replaces the undrained shear strength in terms of providing a normalising quantity for τ_f and σ'_{v0}. The interface friction angle must also be considered, although spanning a relatively small range for typical pile surfaces.

The area ratio of open-ended driven piles, relating the cross-sectional area of steel to the gross cross-sectional area of the pile, affects the external soil displacement and hence the stress changes in the soil around the pile. For fine-grained soils this will influence the extent of the excess pore pressure field generated during pile installation, and hence the time scale of excess pore pressure dissipation and increase in shaft friction (Randolph 2003), as discussed further below.

It has always been intriguing that the database of pile load tests in clay does not show discernible differences in shaft capacity depending on whether the pile was open-ended or closed-ended (including solid), even though the external stress changes during installation must be affected to some degree. However, cavity expansion analysis shows that, for typical wall thickness ratios (or ratios of D_{eq}/D), the expansion stress is not significantly less (perhaps 15 to 20 %) than for a solid pile, and also some proportion of the total stress increase is lost during the consolidation process, moderating the difference. By contrast, suction caissons have much higher D/t ratios, and even more so when allowance is made for some of the soil displaced by the tip entering the caisson. Hence the final shaft friction will be lower than for a driven pile in similar soil (Randolph 2003).

For sands, the area ratio, A_r (or more precisely the effective area ratio, Lehane et al. 2005) influences the magnitude of the radial stresses established in the soil as the pile tip passes, and which subsequently decrease as the pile is driven deeper. A subtle difference among the different cone-based design methods is the manner in which the area ratio is implemented in the estimation of shaft friction (Schneider et al. 2008). In the Imperial College method (Jardine et al. 2005), the shaft friction is taken to degrade from its initial value as a function of the distance, h, normalised by the equivalent diameter, D_{eq}, (where $D_{eq}^2 = A_r D^2$). By contrast, in the UWA approach (Lehane et al. 2005), while the area ratio is used to modify the ratio of radial stress (close to the pile tip) to q_c, the subsequent decay in radial stress is expressed as a function of h/D. These two approaches result in quite similar forms of expression for the shaft friction, but the underlying conceptual models differ. Friction degradation according to h/D, rather than h/D_{eq} seems more logical, since the soil at depths shallower than the pile tip no longer has any knowledge of (or influence from) the area ratio in respect of subsequent densification within the shearing zone adjacent to the pile. The influence of the area ratio on the initial radial stress is also supported by analysis (White et al. 2005).

It is acknowledged that the use of the distance, h, to quantify friction degradation is really a surrogate for the number of shear stress cycles to which the soil is exposed, since it is the cyclic shearing that provides the underlying mechanism (White and Lehane 2004). Normalisation by D pre-supposes that piles of different diameter are subjected to broadly similar numbers of hammer blows per diameter advance. Relatively easy or hard driving will affect the rate of friction degradation with h/D. Indeed, ad hoc experimental evidence suggests that hard driving, with limited advance per blow, can cause greater harm due to friction degradation than any benefit obtained by advancing the pile tip further.

A missing element from current friction degradation models is any quantified minimum value of shaft friction, below which degradation ceases, because the density of the sand at the pile-soil interface has reached its maximum value for the particular effective stress level. This type of stabilisation has been explored through constant normal stiffness (CNS) shear box testing, and the framework of a predictive model proposed, based on concepts of critical state soil mechanics (DeJong et al. 2006). The secondary influence on the rate of degradation of the cavity stiffness, which is proportional to G_{max}/D, would probably be too elusive to extract from the database of pile load tests, but offers a suitable basis with which to refine predictive approaches.

2.2 *Post-installation consolidation*

The increase in pile shaft capacity following installation is amenable to analysis, since it corresponds to dissipation of excess pore pressure through (primarily) radial consolidation. Analytical solutions for radial consolidation, following insertion of a solid object such as a pile or piezocone, give the normalised excess pore pressure, $U = \Delta u/\Delta u_{initial}$, as a function of a non-dimensional time $T = c_v t/D^2$, where c_v is the consolidation coefficient (Randolph and Wroth 1979). The solution depends on the rigidity index, G/s_u, associated with cavity expansion (i.e. the penetration phase). For $G/s_u \sim 100$, the relationship between U and T may be approximated by

$$U = \frac{1}{1+(T/T_{50})^{0.75}} \qquad (1)$$

where T_{50} is the time for 50 % dissipation and is about 0.6. The corresponding value of T_{90} is about 12.

The consolidation coefficient is that associated with radial consolidation and, just as for piezocone dissipation, is biased more towards conditions of swelling, which occurs in the mid to far field, rather than the compression and loss of water content that occurs close to the pile. For an open-ended pile or caisson, the outer diameter, D, should be replaced by the equivalent diameter, D_{eq}, so that T is defined as (Randolph 2003)

$$T = \frac{c_v t}{D_{eq}^2} = \frac{c_v t}{A_r D^2} \qquad (2)$$

There is very limited field data with which to compare the solution for excess pore pressure dissipation, although some recent studies have reported increases in pile driving resistance

(Dutt and Ehlers 2009), and of suction caisson extraction resistance (Colliat and Colliard 2010).

Figure 1 shows a comparison of the radial consolidation solution with the driving resistance data from Dutt and Ehlers, taken from sites off the coast of West Africa and in the Gulf of Mexico. The long term driving resistance was estimated directly from the API design guidelines, since the longest re-drive delay was only 8 days (West Africa) to 12 days (Gulf of Mexico). The data were plotted together, even though the pile diameters varied between 2.7 m (West Africa, diameter to wall thickness D/t = 40, so D_{eq} = 0.85 m) and 2.1 m (Gulf of Mexico: D/t = 48, so D_{eq} = 0.6 m). The initial driving resistance was around 20 % of the (estimated) long term resistance, so the analytical consolidation solution has been adjusted to give a proportion of long term resistance of 0.2 + 0.8U. The solution matches the Gulf of Mexico data reasonably, with a plausible consolidation coefficient of c_v = 20 m^2/yr. The data from West Africa do not show a clear trend, but are mostly bounded by a theoretical curve for c_v = 100 m^2/yr. Although this seems quite high, these piles were driven to a depth of 150 m, twice the depth of the Gulf of Mexico piles, and so is reasonable as an upper bound.

Data from suction caissons from offshore West Africa are shown in Figure 2. The suction caissons were extracted (by pumping water into them) at different periods following installation (Colliat and Colliard 2010). The diameters ranged between 3.8 and 8 m, and penetration depths from 16.5 to 20.5 m. Although much greater diameter than typical driven piles, the values of wall thickness were only 20 or 25 mm. Allowing for only 50 % of the soil displaced being pushed outwards (Zhou and Randolph 2006), the equivalent diameters are only 0.28 to 0.45 m.

The relative increase in shaft resistance has been obtained by normalising by the original shaft resistance. The longest elapsed time was 1260 days, where the reported shaft resistance was 2.03 times the installation value (the data point is plotted at a reduced time of 100 days, in order to limit the time axis). All data points on Figure 2 have been plotted after first scaling the actual time by $(0.3/D_{eq})^2$ in order to give a common basis of comparison. Inevitably there is some scatter in the data, but the theoretical consolidation curve for c_v = 10 m^2/yr (and D_{eq} = 0.3 m) lies within a factor of about 2 for all but one datapoint. The coefficient of consolidation seems reasonable, given that the average depth is almost an order of magnitude lower than for the driven piles in Figure 1.

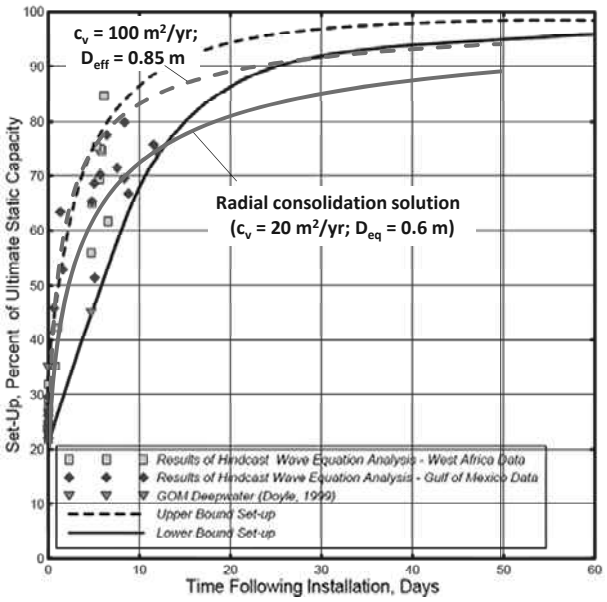

Figure 1 Increase in pile shaft capacity with time following driving (field data and original figure from Dutt and Ehlers 2009).

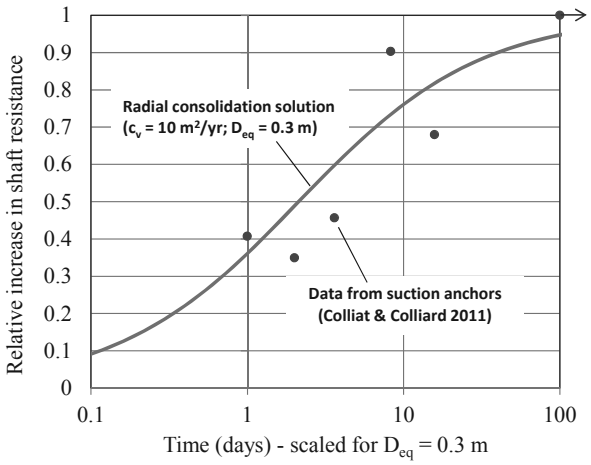

Figure 2 Increase in suction caisson extraction resistance with time following installation.

The time scale of consolidation reported by Colliat and Colliard (2010) is similar to that noted by Jeanjean (2006), for suction caissons with diameters 2.9 to 3.7 m (equivalent diameters of 0.39 to 0.53 m). Unfortunately, though, the latter dataset did not include any short term restart or retrieval data, with the earliest being after a time delay of 50 days (equivalent to 16 days for D_{eq} = 0.3 m). As such, all cases showed relative increases in excess of 50 %. The average long term (~1000 day) increase in shaft resistance was only 75 %, compared with 100 % for the West Africa suction caisson data.

It is perhaps disappointing that greater use is not made of rigorous consolidation analysis in estimating the time scale for the increase in shaft resistance of piles and suction caissons. Commentary on the topic is partly obscured by musings on thixotropy, which may play a role but with no guidance provided on how to scale from laboratory to field. Ultimately the shaft resistance results from the increase in normal effective stress, which is adequately modelled by consolidation analysis.

2.3 *Axial load-displacement response*

In the offshore industry it is customary to use load transfer methods to evaluate the axial load-displacement response. Non-linear load transfer curves allow the full pile response to be evaluated, from the initial quasi-linear response right up to failure. It is instructive, though, to consider the form of the load transfer curves, and elastic solutions for the complete pile that are applicable at low load levels.

Analytical solutions for axial pile response abound, with gradually increasing degree of sophistication, starting with Murff (1975) for the case of a linear load transfer stiffness, k_a, uniform with depth. Randolph and Wroth (1978) related the load transfer stiffness to the soil shear modulus, G, and extended the solution in an approximate manner to consider a linear variation of modulus with depth. This was later extended in a more rigorous manner by Guo and Randolph (1997) for power law variations of modulus with depth, and by Mylonakis and Gazetas (1998) for layered profiles, and with allowance for interaction effects between piles.

The solutions for uniform soil modulus with depth may be expressed in the generic form of

$$K_{axial} = \frac{P_t}{w_t} = S\frac{K_b + S\tanh(\mu L)}{S + K_b\tanh(\mu L)} \qquad (3)$$

with

$$\mu L = \sqrt{\frac{k_a}{(EA)_p}}L \quad \text{and} \quad S = \frac{(EA)_p}{L}\mu L = \sqrt{(EA)_p k_a} \qquad (4)$$

where P_t and w_t are the load and displacement at the top of the pile, K_b is the base stiffness (P_b/w_b), L the embedded pile length and $(EA)_p$ the cross-sectional rigidity of the pile. The solution may be extended for linear variation of modulus with depth by pre-multiplying the tanh(μL) term in the numerator by ρ, the ratio of average modulus to that just above the pile base (Randolph and Wroth 1978); for layered profiles, the base stiffness, K_b, can be replaced by the load-displacement stiffness of the pile segment below the one under consideration, nesting subsequent layers in the same way.

The load transfer stiffness, k_a, (ratio of axial load transfer per unit length of pile to the local axial displacement) may be related to the soil shear modulus, G, by

$$k_a = \frac{2\pi}{\zeta} G \text{ where } \zeta \sim \ln\left(\frac{2L}{D}\right) \sim 4 \quad (5)$$

Randolph and Wroth (1978) provided more explicit guidance on the parameter ζ, which arises due to a logarithmic singularity in integrating the shear strains around the pile. However, within the accuracy to which G may be determined, a value of 4 is sufficiently accurate for piles of moderate L/D.

The ratio of shear strain in the soil adjacent to the pile to the normalised displacement, w/D, is given by ζ/2 (i.e. about 2). This leads to a first estimate for the pile displacement required to mobilise full shaft friction as $w_f/D \sim 2\tau_f/G$ (where τ_f is the limiting shaft friction), which would fall in the range 0.5 to 2 % for G/τ_f of 100 to 400. For a hyperbolic soil response where the secant shear modulus decreases inversely with the strength mobilisation, τ/τ_f, the parameter ζ may be replaced by (Kraft et al. 1981)

$$\zeta \sim 4 - \ln(1-\psi) \text{ where } \psi = R_f \frac{\tau}{\tau_f} \quad (6)$$

with the hyperbolic parameter, R_f, typically around 0.9 to 0.95. This gives a reduction in secant load transfer stiffness by a factor of approximately 2 between low and high shaft friction mobilisation. More general forms of hyperbolic soil model, such as suggested by Fahey and Carter (1993), may be integrated to provide alternative estimates for the evolution of the load transfer stiffness.

The generic form of axial load transfer curves suggested in the offshore guidelines are consistent with this reduction in secant stiffness, with normalised ratios of $(\tau/\tau_f)/(w/w_f)$ that reduce from 1.875 to unity. In a welcome step forward, the latest version of the API guidelines (API 2011) now recommends a similar shape of load transfer curve, and mobilisation displacement, w_f, for sand as for clay, replacing the previous recommendation of 2.5 mm for sand (an anachronism based on experimental data for relatively small pile diameters). Jeanjean et al. (2010) outlined the logic for mobilisation distances for sand, with correlations for G/σ'_{v0} and τ/σ'_{v0} suggesting values around 0.5 % of the diameter, but experimental data generally grouped above 1 % of the diameter. The net result was to propose a similar range for the displacement, w_f, to mobilise failure, for both sand and clay, in the range 0.5 to 2 %.

The underlying theoretical link between the load transfer stiffness and the soil shear modulus should, however, be borne in mind. Where values of small strain shear modulus are available, it would be more sound, theoretically (particularly for assessing dynamic stiffness), to link the initial load transfer gradient to the small strain shear modulus of the soil. Thus the initial gradient should be

$$\left(\frac{d\tau}{dw}\right)_{initial} \sim \frac{G_0}{2D} \quad \text{or} \quad (k_a)_{initial} \sim 1.5G_0 \quad (7)$$

The analytical solution for the pile head stiffness allows the effect of pile compression (or extension), which is controlled by the quantity μL, to be explored. For a stiff pile (high ratio of $(EA)_p/L$ to k_aL), the overall pile head stiffness, K_{axial}, is just the sum of the shaft and base stiffness acting in parallel (i.e. $K_b + k_aL$). However, as μL increases, tanh(μL) approaches unity and the pile head stiffness asymptotes to

$$K_{axial} = S = \sqrt{(EA)_p k_a} \sim 1.25\sqrt{(EA)_p G} \quad (8)$$

The above relationship is useful for estimating the dynamic stiffness of a pile (substituting G_0 for G). It also provides a guide to evaluate the load at which failure first occurs at the pile-soil interface, which may be expressed as

$$\frac{P_{slip}}{Q_{shaft}} = \frac{1}{\mu L} = \frac{1}{L}\sqrt{\frac{(EA)_p}{k_a}} \sim \frac{0.8}{L}\sqrt{\frac{(EA)_p}{G}} \quad (9)$$

This has particular relevance for assessing the cyclic robustness of piles under axial loading. There is substantial experimental evidence that suggests degradation in load transfer under cyclic loading occurs very rapidly once local slip has occurred (Erbrich et al. 2010). Stability diagrams for cyclic loading are generally expressed in terms of the cyclic and mean loads applied at the pile head, normalised by the pile (shaft) capacity, as illustrated in Figure 3 (Poulos 1988, Puech et al. 2013). However, such diagrams do not take account of the relative compressibility (or extensibility) of the pile within the soil. For high ratios of $(EA)_p/GL^2$, slip will occur at relatively low proportions of the shaft capacity, which will allow degradation to occur, reducing the shaft friction in the upper part of the pile to a cyclic residual level.

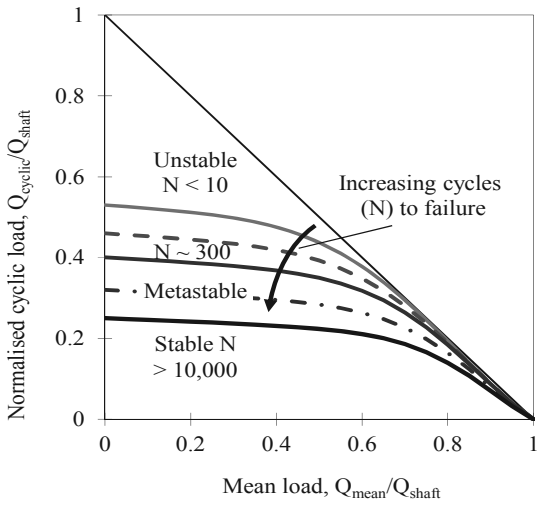

Figure 3 Typical form of cyclic stability diagram.

Cyclic stability diagrams are therefore of limited use for a complete pile (unless it is relatively stiff), although they are useful to describe the soil response at a local level, rather like similar diagrams for element tests (Andersen 2009). An alternative approach is to use shakedown theory to arrive iteratively at a profile of mean and cyclic shear stresses down the pile that all lie within the stable zone of a stability diagram (based on soil element response). Residual shaft friction conditions should first be assumed throughout the upper region of the pile where slip occurs under the maximum operational loading.

2.4 *Post-peak strain softening*

Axial compression or extension of the pile leads to non-uniform mobilisation of shaft friction down the length of the pile, with slip between pile and soil generally being initiated at the mudline and gradually propagating down the length of the shaft. Any strain softening in the load transfer response will therefore allow a form of progressive failure, such that the maximum shaft resistance will be less than the ideal value for a hypothetical rigid pile.

Alternative forms of load transfer curve are shown in normalised form in Figure 4, with the linear degradation to 70 % of peak shaft friction being consistent with API and ISO design guidelines for clay. A difficult consideration is how to scale the degradation response from laboratory to field scale, and the extent to which a given degree of degradation should be based on absolute displacement or displacement scaled to pile diameter. Even though the degradation occurs locally at the pile-soil interface, the surrounding stress field (and even the width of the main shearing zone) is affected by the pile size, so that scaling with pile diameter seems at least partly justified. In some soil types, much more significant degradation can occur (Erbrich et al. 2010), possibly occurring over rather greater displacement than the 1 % of pile diameter suggested in offshore design guidelines.

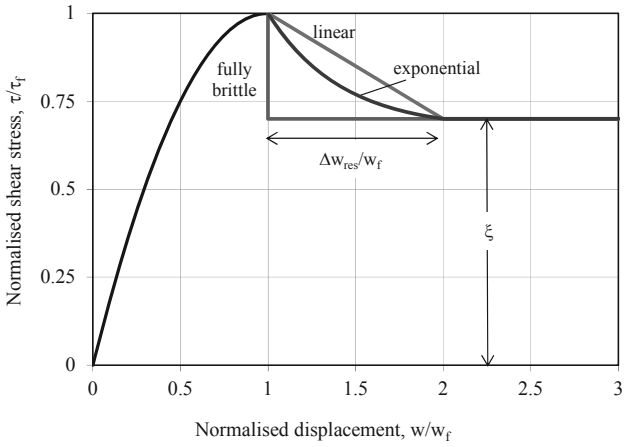

Figure 4 Alternative forms of post-peak softening in axial load transfer curves.

The actual shaft resistance, Q_s, may be expressed as a proportion, R_{pf}, of the ideal shaft capacity, Q_{shaft}:

$$Q_s = R_{pf} Q_{shaft} \quad \text{where } Q_{shaft} = \pi D L \bar{\tau}_f \tag{10}$$

The value of R_{pf} will be a function of the degree and brittleness of strain softening and the compressibility of the pile.

An analytical solution for the extreme case of 'instant' strain softening was given by Murff (1980), who expressed the reduction factor, R_{pf}, as a function of the strain-softening ratio, $\xi = \tau_{res}/\tau_f$, and a non-dimensional pile compressibility, π_3. The latter quantity may be shown to be identical to μL. For strain softening over a finite distance, Δw_{res}, Randolph (1983) proposed an alternative non-dimensional pile compressibility or compliance, C, substituting the displacement to failure, w_f, for the displacement from peak to residual, Δw_{res}. Numerical experiments suggest, however, that a more robust measure of pile compliance, in respect of progressive failure, is the total displacement to residual, i.e. $w_f + \Delta w_{res}$, with C defined as:

$$C = \frac{\pi D \tau_f L^2}{(EA)_p (w_f + \Delta w_{res})} \tag{11}$$

With this definition, the reduction factor can be approximated as

$$R_{pf} \sim \xi + (1-\xi)\tanh\left(\frac{1}{\sqrt{C}}\right) \tag{12}$$

as illustrated in Figure 5.

This expression provides an initial estimate to assess the extent to which progressive failure may reduce the net shaft resistance. The actual reduction factor will depend on the precise form of the load transfer curve, particularly in respect of degradation, and should therefore be evaluated through numerical analysis. A detailed investigation of the performance of steel jacket structures in Gulf of Mexico hurricanes found that the one case where axial pile failure occurred could be explained by progressive failure using the API (2011) recommended form of load transfer curve with degradation to 70 % of peak friction (Gilbert et al. 2010).

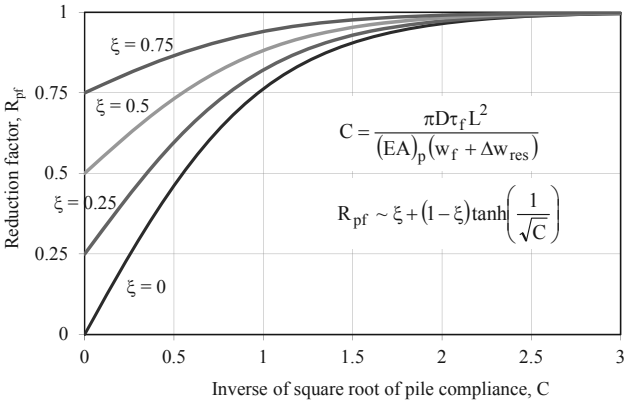

Figure 5 Reduction factor due to progressive failure.

2.5 *Lateral pile resistance – clay*

Design methodology for the lateral response of piles is almost universally based on load transfer approaches. These are well-suited to capture the significantly non-linear soil response, particularly in the upper few diameters of the pile. However, the proposed load transfer curves are labyrinthine in formulation and with no obvious link to any analytical basis. Jeanjean (2009) has argued for an overhaul of the API guidelines for soft clay conditions, proposing an alternative formulation based on a combination of (centrifuge) model test data and finite element analysis, but with the ultimate lateral resistance at any depth linked to upper bound solutions (Murff and Hamilton 1993).

The Murff and Hamilton solution addresses soil failure at shallow depth, based on a three-dimensional conical wedge mechanism. Below the wedge, the lateral resistance is limited by plane strain flow around the cylindrical pile (Randolph and Houlsby 1984, Martin and Randolph 2006). The solutions take account of the relative roughness between pile and soil, with the limiting (plane strain) resistance at depth varying with the friction ratio, α, as:

$$\frac{P_u}{s_u D} = N_p \sim 9.14 + 4.14\alpha - 1.34\alpha^2 \tag{13}$$

From a design perspective, a simple linear fit of $N_p = 9 + 3\alpha$ is sufficiently accurate, being generally about 3 % conservative apart from at the limit of a fully rough pile when it rounds to 12 instead of 11.94.

There is an incompatibility at the transition depth between the wedge and the plane strain flow, but this does not appear to have a significant effect on the overall pile resistance, judging by comparisons with full finite element analyses. The discontinuity can be removed by allowing a gradual transfer

from the wedge mechanism to the flow mechanism (Klar and Randolph 2008).

Although the Murff and Hamilton upper bound solution treats the conical wedge mechanism as a whole, to provide an overall lateral resistance for that section of the pile, they explored suitable variations of N_p with depth, z, that fitted the overall upper bound resistance for piles of different embedment. This led to proposed factors of

$$N_p = N_1 - N_2 e^{-\xi z/D} \quad (14)$$

with ξ adjusted for different strength profiles idealised as $s_u = s_{um} + \rho z$, according to

$$\xi = \mathrm{Min}\left(0.25 + 0.05\frac{s_{um}}{\rho D},\ 0.55\right) \quad (15)$$

The value of N_p therefore increases from a surface value of $N_1 - N_2$, to a limiting value at depth of N_1 (corresponding to Equation (13)). Assuming a double sided mechanism (with negative excess pore pressures behind the pile causing the soil to move with the pile) the Murff and Hamilton mechanism leads to an almost constant value of 5 for N_2. Thus the surface value of N_p increases approximately linearly with α from about 4 for a smooth pile ($\alpha = 0$) to 7 for a rough pile ($\alpha = 1$).

Jeanjean (2009) has recommended adoption of $N_1 = 12$ and $N_2 = 4$, without consideration of the friction ratio, α. Even for fully rough conditions this is slightly optimistic in respect of the surface value of N_p (8 instead of the upper bound value of 7). Also, as commented by Murff and Hamilton (1993), the additional resistance provided by a fully rough pile compared with a smooth pile "*would seem to be particularly susceptible to degradation due to cyclic loading, and thus it may not be prudent to count on it for design*". A compensating factor to this (intuitive) consideration is the gradual hardening that occurs due to consolidation between periods of cyclic perturbation (Zhang et al. 2011). The net effect of this is that the post-cyclic monotonic pile responses showed slight increases in resistance for a given pile displacement. Similar hardening was observed in centrifuge model tests simulating the interaction of steel catenary risers with the seabed (Hodder et al. 2013).

Equally important for lateral pile design is the mobilisation of lateral resistance with displacement. Variations in the stiffness at small displacements for elements at some depth down the pile can have a significant effect on the pile head response. The current API and ISO guidelines for load transfer curves appear too soft at moderate displacements (Jeanjean 2009), although the initial data point, with $P/P_u = 0.23$ for a displacement of $y = 0.1y_c = 0.25\varepsilon_{50}D$, implies a rather high stiffness. Here ε_{50} is defined as the strain in a (triaxial) compression test at half the failure deviator stress, which is equivalent to $s_u/3G_{50}$. Hence for $P_u = 9s_uD$, the initial gradient is $P/y = 9\times0.23\times3G_{50}/0.25 = 25G_{50}$.

Theoretical solutions for the load transfer response, either based on an analogy with cavity expansion or closed form solutions (Baguelin et al. 1977), lead to a gradient of $k_{py} \sim 4G$, and hence a maximum gradient of $4G_0$. Applying this as a limit at small displacements to the hyperbolic tangent function suggested by Jeanjean (2009) leads to

$$\frac{P}{P_u} = \mathrm{Min}\left[\tanh\left(0.01\frac{G_0}{s_u}\sqrt{\frac{y}{D}}\right),\ \frac{4G_0}{P_u}y\right] \quad (16)$$

For $P_u = 12s_uD$, the transition point occurs at $y/D = 0.0009$, so $P/P_u = 0.0003G_0/s_u$ or 0.12 for $G_0/s_u = 400$.

Although Jeanjean's study was for soft clays, in principle the same general approach should be applicable to stiff clays but with some caveats:

- Where stiff clays occur at the seabed surface, a gap is much more likely to develop than for soft clays (since higher $s_u/\gamma'D$, and much greater suctions required to be sustained in order to prevent a gap forming). As such, the surface factor ($N_1 - N_2$) should be halved, while retaining the same limiting (plane strain) value of N_p.
- A lower friction ratio, α, is likely to be appropriate, just as for axial shaft friction.

2.6 *Lateral pile resistance – sand*

For sand, design recommendations for limiting lateral resistance still rely on a limit equilibrium calculation for a putative passive wedge of soil failing ahead of the pile. There is also an overriding maximum limiting resistance, proportional to depth, although this is extremely high (such that, in practice, it would not be reached shallower than depths exceeding 15 pile diameters). The resulting profiles of limiting resistance are not consistent with results from numerical modelling, or even with empirical data that appear to follow a linear trend, below a depth of about 1 diameter, that is broadly proportional to the square of the passive earth pressure coefficient, K_p.

However, any design approach requiring what is ultimately a bearing resistance, but is couched in terms of friction angle, ϕ', suffers from the problems of (a) how to 'measure' ϕ', and (b) the need to adjust ϕ' according to the resulting implied effective stress level. Typically values of ϕ' must be deduced from the results of cone penetration tests. It is therefore far more logical to link the lateral pile resistance directly to the cone resistance, following the path taken for axial pile capacity.

Empirically based approaches that express the lateral pile resistance as a function of the cone resistance have been proposed for carbonate sands (Wesselink et al. 1988, Novello 1999, Dyson and Randolph 2001). Recently, a numerical study has been undertaken by Suryasentana and Lehane (2013) to provide a more theoretical link between lateral pile resistance and cone resistance, the latter being simulated as spherical cavity expansion. Material properties were based on those for a typical silica sand.

Systematic dimensional analysis, with a parametric study covering a wide range of the various dimensionless groups, allowed relationships to be developed between normalised values of pile resistance, cone resistance, depth and lateral displacement. The eventual relationship incorporated an exponential term to give a true limiting lateral resistance at large displacement. The lateral resistance was then expressed as (Suryasentana and Lehane 2013):

$$\frac{P}{\sigma'_{v0}D} = 2\left(\frac{q_c}{\sigma'_{v0}}\right)^{0.68}\left(\frac{z}{D}\right)^{0.61}\left[1 - \exp\left(-8.9\left(\frac{z}{D}\right)^{-1.1}\left(\frac{y}{D}\right)^{0.94}\right)\right] \quad (17)$$

This study represents an important step towards a more rational approach to the estimation of load transfer responses for lateral pile design in sand. The rather gradual development of the ultimate resistance (the terms outside the square bracket in Equation (17)) is in stark contrast to the hyperbolic tangent relationship in the current design guidelines, which leads to the ultimate resistance being mobilised at displacements of 1 or 2 % of the pile diameter.

3 SHALLOW FOUNDATIONS

Design guidelines for shallow foundations that are provided in the main geotechnical guides (ISO 2003, API 2011) have developed from guidance for temporary mudmat foundations to support steel jacket structures, prior to pile installation. Large

gravity foundations and spudcan foundations are dealt with in separate documents focusing respectively on concrete structures and mobile drilling rigs. The main geotechnical guidelines focus on bearing capacity, based on classical solutions for strip foundations, modified using heuristic adjustment factors for foundation shape and embedment, and the influence of horizontal and moment loading.

The largest use of shallow foundations offshore is now for deep water subsea systems, where they are widely used for pipeline end terminations and manifolds. In the main, the seabed sediments in deep water comprise fine-grained soil, with relatively low strength at mudline. The foundations are steel mats, generally rectangular in plan with shallow skirts, and with a high cost incentive to minimise the size to allow installation from pipe-lay vessels. The emphasis in design for geotechnical capacity is on horizontal and moment loading from the attached pipeline and jumpers, rather than on vertical bearing capacity.

Along with the changing nature of shallow foundation applications, the last decade or so has seen increasing analytical emphasis on the development of failure envelopes in vertical (V), horizontal (H) and moment (M) load space. The most recent API guidelines (API 2011) now include a commentary that permits (encourages would be too strong a word) the use of failure envelopes as an alternative approach; this is timely since it suits better application to shallow foundations for subsea systems, where failure tends to be by sliding or overturning.

Table 1 Summary of analytical and numerical studies of failure envelopes for shallow foundations for undrained conditions

Reference	Load cases	Max $\rho B/s_{u0}$ or $\rho D/s_{u0}$	Max embed. depth d/B	Strip, Circle, Rectangle	Tension, Closed form (*)
Bransby-Randolph 1998	VHM	∞	0	S	Y*
Bransby-Randolph 1999	VHM	6	0.17	S	Y*
Houlsby-Puzrin 1999	VHM	0	0	S	N*
Taiebat-Carter 2000	VHM	0	0	C	Y*
Taiebat-Carter 2002	VM	0	0	C	N
Gourvenec-Randolph 2003	HM	10	0	SC	Y
Randolph-Puzrin 2003	VHM	6	0	C	Y*
Finnie-Morgan 2004	HT	0	0	SCR	-
Yun-Bransby 2007	HM	200	1	S	Y
Gourvenec 2007a	VHM	0	0	R	N*/Y
Gourvenec 2007b	VHM	6	0	SC	Y
Gourvenec 2008	VHM	0	1	S	Y
Bransby-Yun 2009	VHM	200	1	S	Y
Yun et al. 2009	VHT	0	0	SCR	-
Taiebat-Carter 2010	VHM	0	0	C	N
Murff et al. 2010	HT	0	0.05	R	-
Gourvenec-Barnett 2011	VHM	6	1	S	Y
Feng et al. 2013	Full 3D	10	0.2	R	Y*

Table 1 provides a summary of some of the solutions published over the last fifteen years, indicating which include either analytical solutions, or at least closed form algebraic expressions for failure envelopes. As is the nature of analysis, idealisations of the real system have to be made, with each study tending to focus on a different set of restrictions. There is a wealth of information in the various contributions, to which justice cannot be done here. Instead, one or two salient points will be commented on and suggestions made for practical approaches for use in design.

The focus is on rectangular foundations, with relatively shallow skirts, since these are of particular relevance to deep water developments. A schematic of the problem is shown in Figure 6. In the most general case, six independent loads and moments may act on the foundation, and the dimensionless groups that need to be considered include the foundation aspect ratio, B/L, embedment ratio, d/B, and normalised soil strength gradient, $\kappa = \rho B/s_{u0}$. (Relevant ratios for a circular foundation of diameter, D, where the loading can generally be simplified to the three components, V, H and M, in the plane containing the resultant horizontal load, are d/D and $\rho D/s_{u0}$.)

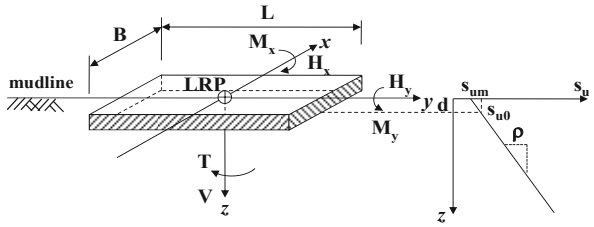

Figure 6 General loading applied on a rectangular skirted foundation with linearly varying soil strength.

Even though typical embedment ratios of subsea system foundations are quite low, there can still be an appreciable increase in capacity. Design guidelines simplify the effects of aspect ratio and embedment into separable additive factors, whereas in reality the depth factor is itself a function of the embedment ratio (Salgado et al. 2004) and also the strength gradient factor, κ. The depth correction factor in API (2011) is deliberately conservative (Figure 7), expressed as:

$$d_c = 1 + 0.3\arctan(d/B) \tag{18}$$

with B replaced by the effective width, B', for foundations where no tensile stresses are permitted.

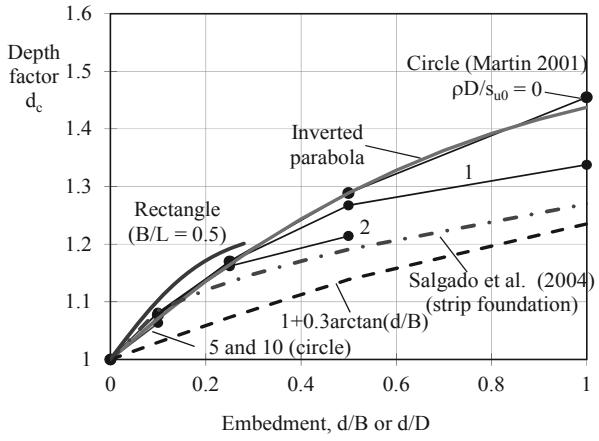

Figure 7 Depth correction factors for different shaped foundations.

This expression provides a lower bound to those derived analytically, even for a strip foundation. The correction factor from Salgado et al. (2004) for strip foundations, which varies with the square root of d/B, is shown in Figure 7 for comparison. Also plotted are depth factors deduced from lower bound results for circular foundations for a range of $\rho D/s_{u0}$

(Martin 2001). These show the effect of $\rho D/s_{u0}$ (κ), with the depth factor reducing with increasing κ as d/D increases, relative to the factor for homogeneous (uniform strength) soil.

In the range relevant for subsea systems, the results for different values of κ converge, and can be fitted by an inverted parabola with apex at $d_c = 1.5$ for d/D = 2. However, these are still lower than for a rectangular foundation with B/L = 0.5, according to results of 3D finite element analyses (Feng et al. 2013). These give an initial gradient for the depth factor of greater than unity with respect to d/B, and a significant 17 % increase in bearing capacity for d/B = 0.2.

For circular foundations, it is possible to develop three-dimensional failure envelopes in V-H-M space. Failure envelopes are most effectively expressed in normalised units, $v = V/V_u$, $h = H/H_u$ and $m = M/M_u$, where the subscript "u" indicates the limiting uniaxial resistance (e.g. for V, with M = H = 0). A promising form for foundations that can withstand tensile stresses is (Taiebat and Carter 2000):

$$v^2 + \left[m\left(1 - 0.3h\frac{m}{|m|}\right)\right]^2 + h^3 - 1 = 0 \qquad (19)$$

which gave a reasonable fit to finite element results for a circular foundation resting on the surface of homogenous soil. An improved failure envelope, though not expressed in algebraic form, was discussed by Taiebat and Carter (2010). The various powers and coefficients would need adjusting for different foundation shapes, embedment ratios and normalised shear strength gradient.

There is little prospect of any simple way of expressing a failure envelope for full three-dimensional loading applied to a rectangular foundation. Instead, a simplified approach has been proposed recently (Feng et al. 2013), taking advantage of the relatively low mobilisation of the uniaxial vertical capacity for subsea system foundations, where unfactored values of v will rarely exceed about 0.3.

Table 2 Steps in design process for subsea system foundations

Step	Details
1	For given foundation geometry evaluate s_{u0} and non-dimensional quantities B/L, d/B and κ
2	Evaluate uniaxial capacities for vertical, horizontal, moment and torsional loading
3	Reduce ultimate horizontal, moment and torsional capacities to maximum values available, according to mobilised (design) vertical capacity, $v = V/V_u$
4	For given angle, θ, of resultant horizontal load, H, in the horizontal plane, evaluate corresponding ultimate horizontal capacity, and similarly for ultimate moment capacity
5	Evaluate reduced ultimate horizontal and moment capacities due to normalised torsional loading
6	Evaluate extent to which applied (design) loading falls within H-M failure envelope, and thus safety factors on self-weight V, live loading H, M, T or material strength s_{u0}

The steps in the approach are tabulated in Table 2. In common with most failure envelopes, the uniaxial capacities are first evaluated, providing a first indication of the relative mobilisation for each of the 6 degrees of freedom. Using interaction diagrams for v-h_x, v-h_y, v-m_x, v-m_y and v-t, reduced allowable values of H_x, H_y etc are deduced, according to the applied v. Separate interaction diagrams for h_x-h_y and m_x-m_y (with the ultimate values for each component reflecting the reduction from the previous step) then allow estimates of the maximum *resultant* H and M, for the given loading angles in the H and M planes. These maximum values are then reduced further according to the mobilised torsion, t, by considering h-t and m-t interaction diagrams. The logic behind the various steps is to arrive at a final h-m failure envelope that has already taken full account of the mobilisation ratios for vertical and torsional modes of failure.

Full details of these steps are described by Feng et al. (2013) for rectangular skirted foundations that can withstand tensile stresses. The failure envelopes involving v are based on generic shapes proposed in the literature, for example

$$\begin{aligned} v &= v^* + (1 - v^*)\sqrt{1 - h^q} \quad \text{for } v > v^* \text{ else } h = 1 \\ v &= (1 - m)^p \end{aligned} \qquad (20)$$

with v-t interaction following a similar type of envelope as for v-h interaction. Values of the transition v (v^*) and the exponents q, p have been fine-tuned for rectangular foundations with B/L in the region of 0.5, and take account of the loading direction relative to the rectangular foundation and (for p) the normalised shear strength gradient.

Other failure envelopes, for h_x-h_y, h-t etc are elliptical in form, for example

$$h_x^a + h_y^b = 1 \qquad (21)$$

again with each envelope fitted to results from 3D finite element analyses, expressing the exponents a and b as functions of the dimensionless input variables.

The final form of h-m failure envelope is similar in nature to that proposed by Taiebat and Carter (2000), although now without the term for v (which has been allowed for separately):

$$\left(m_d \frac{m_d}{|m_d|}\right)^q \left(1 - \alpha h \frac{m_d}{|m_d|} + \beta h^2\right) + h^2 - 1 = 0 \qquad (22)$$

where the parameters q, α and β are expressed as functions of κ and, in the case of α, as a function of the resultant horizontal loading direction, $\theta = \arctan(H_x/H_y)$ (Feng et al. 2013). It was found that the shape of the failure envelope became insensitive to the embedment depth provided the moment was expressed as if the load reference point was shifted from mudline to skirt tip depth, d; thus $M_d = M + Hd$.

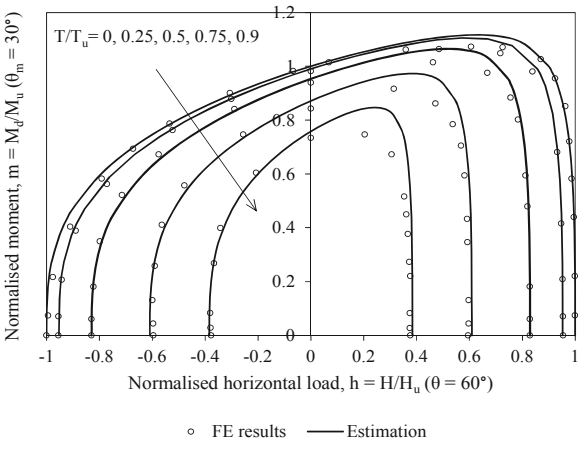

Figure 8 Example comparison between estimated failure envelopes for different torsion mobilisation ratios and FE results (Feng et al. 2013).

Examples of the fit between results of individual finite element computations and the estimated failure envelopes are

shown in Figure 8, for a case of a surface foundation on homogeneous soil, with resultant horizontal loading at 60 º to the x-axis. The failure envelopes and FE results correspond to five different torsion mobilisation ratios. The quality of fit is reasonably good, although with slight over prediction of the maximum moment capacity at high levels of torsion.

An example foundation analysis following this approach is presented here, with input data (including factored design loads) tabulated in Table 3 and the resulting failure envelopes and design loading shown in Figure 9. Failure envelopes based on unfactored shear strengths are shown as dashed lines, with the outer (black) envelope corresponding to zero torsion, and the inner (red) envelope after allowing for the applied torsion of 2100 kNm. The solid lines represent failure envelopes after reducing the shear strength by the material factor of 1.58 that is just sufficient to cause failure; again the outer and inner of these two envelopes represent situations with zero torsion and the actual design torsion. The increased mobilisation ratios for v and t, due to factoring the shear strength, reduce the maximum values of H and M for the failure envelopes that allow for the applied torsion by greater factors, respectively 2.1 and 1.8.

Table 3 Input data for example subsea system foundation

Parameter	Value	Units	Design loads	Value	Units
Width, B	8	m	Vert. load, V	1200	kN
Length, L	16	m	Load, H_x	200	kN
Skirt, d	0.6	m	Load, H_y	300	kN
Strength, s_{um}	5	kPa	Moment, M_x	1500	kNm
s_u gradient, k	2	kPa/m	Moment, M_y	-2400	kNm
Skirt friction	0		Torsion, T	2100	kNm

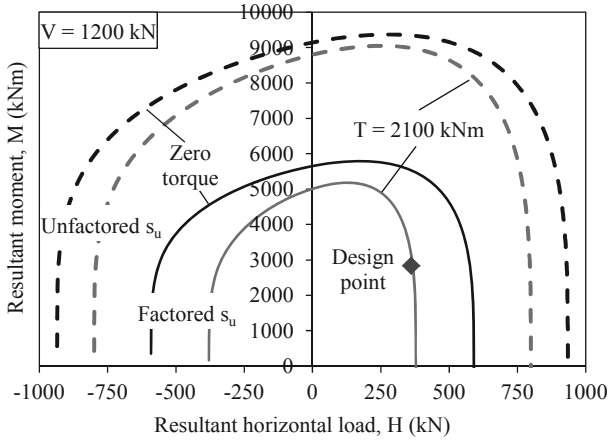

Figure 9 Failure envelopes and design loading for example application.

From a design perspective, optimising the size of shallow foundations for subsea systems requires more sophisticated analysis than the conventional approach for bearing capacity followed in offshore design guidelines. The use of failure envelopes for combined V-H-M loading provides a suitable advance. Depending on the sensitivity of the structure, final design may well involve detailed 2D or 3D finite element analysis, but simpler tools are needed to enable initial sizing.

Design using failure envelopes is modular, with the first step being to evaluate uniaxial failure loads and moments for the relevant degrees of freedom. For circular foundations in-plane loading may generally be assumed, with only three degrees of freedom, unless the torsion is significant. If that is the case, the horizontal capacity should be reduced to compensate (Finnie and Morgan 2004, Murff et al. 2010), and possibly the moment capacity as well. For rectangular foundations all six degrees of freedom need to be considered.

Generic shapes of failure envelope, based on loads normalised by their ultimate uniaxial values, are much less sensitive to foundation shape and embedment ratio, and soil strength gradient, than are the uniaxial load limits. As such, the shapes need not necessarily be fine-tuned. The most awkward shape is the failure envelope in the h-m plane. For planar loading, the approach described by Gourvenec (2007b) is therefore attractive, based on generic failure envelopes in v-m space for different magnitudes of (normalised) horizontal load eccentricity, m/h.

For rectangular foundations, particularly if relatively lightly loaded vertically, the approach outlined in Table 2 offers a simple way forward, maintaining a modular concept where the various interaction diagrams may be fine-tuned to suit particular conditions, if these deviate significantly from those considered by Feng et al. (2013). For example, interaction diagrams based on sustained tensile stresses could be replaced by equivalent ones based on a zero tension condition.

The increasing complexity of subsea systems brings the potential for higher service loads due to thermal and pressure-driven movements of the pipeline and jumper connections. The cost incentive to limit the overall foundation dimensions is therefore driving innovation, both in analysis methods but also in the foundation configuration itself. One such innovation is to include pin-piles at the foundation corners, which can increase the sliding and torsional capacity by a factor of 3 or 4. A simple design approach for such a hybrid foundation has recently been developed, following lower bound principles (Dimmock et al. 2013), and validated through physical model tests (Gaudin et al. 2012). An alternative approach is to design the foundation to slide, hence reducing the magnitudes of horizontal load and moment (Bretelle and Wallerand 2013). Both of these strategies still rely on failure envelopes for different combinations of load and moment, either to ensure adequate capacity, or to evaluate the displacement and rotation paths for sliding foundations.

4 USE OF FAILURE ENVELOPES FOR ANCHORS

In most design applications, failure envelopes are used to establish safe load combinations. However, they may also be used to model the kinematic response during continuous failure. The concept was applied to predict the trajectory of drag embedment anchors by Bransby and O'Neill (1999), successfully simulating centrifuge model tests (O'Neill et al. 2003).

In soft sediments, drag anchors embed to several times the length of their flukes, advancing approximately parallel to the flukes and gradually rotating until the flukes approach the horizontal, signifying reaching their ultimate penetration depth. The anchor chain forms a reverse catenary through the soil, described by an analytical solution expressed in terms of the chain tension, T, and average soil resistance, $\overline{Q}$, between mudline and padeye depth (Neubecker and Randolph 1995). Critical is the angle change between mudline and padeye, which may be approximated as

$$\left(\theta_a^2 - \theta_0^2\right) \sim \frac{2 z_a \overline{Q}}{T_a} \tag{23}$$

where subscripts 'a' and '0' correspond to the anchor padeye and mudline respectively.

Solutions for the final anchor embedment depth and ultimate capacity were initially obtained using simplified limit equilibrium (Neubecker and Randolph 1996) or upper bound (Aubeny et al. 2005, 2008) approaches. The use of a full failure envelope to obtain the relative motions, parallel and normal to the anchor fluke, and rotation, represented a more rigorous treatment.

The form of failure envelope adopted by Bransby and O'Neill (1999) was based on that suggested by Murff (1994):

$$n^q + \left(m^r + s^t\right)^{(1/p)} - 1 = 0 \qquad (24)$$

where n, m and s represent the mobilisation ratios (e.g. $n = N/N_u$) for normal, moment and sliding modes relative to the anchor fluke. Ultimate, uniaxial, limits, N_u, M_u and S_u are typically obtained from a combination of plasticity solutions and finite element analysis, depending on the anchor fluke shape (O'Neill et al. 2003, Aubeny and Chi 2010). Similarly, the various powers may be adjusted to fit different anchor shapes, with q and t typically in the range 3 to 5, and p, r around unity (Bransby and O'Neill 1999, Elkhatib 2006, Yang et al. 2010). The values of q, r and t should not be chosen less than p, in order to guarantee convexity of the failure envelope.

A similar approach was adopted to model the keying of mandrel-installed plate anchors, such as the suction embedded plate anchor or SEPLA (Cassidy et al. 2012, Yang et al. 2012). Combining the chain response with the failure envelope allows the full kinematic response of the plate anchor to be investigated. The position of the padeye relative to the plate centre may then be optimised, minimising loss of embedment during keying or even such as to cause the anchor to dive. A careful finite element based parametric study showed that the original SEPLA design, which incorporated a hinged flap to help limit loss of embedment during keying, was ill conceived (Tian et al. 2013). More recent numerical work has considered sophisticated 3D anchor geometries, investigating how the presence of the shank affects the failure envelope (Wei et al. 2013).

5 FULL-FLOW PENETROMETERS

Full-flow penetrometers, the cylindrical T-bar and spherical ball (Figure 10), were introduced in the 1990s (Stewart and Randolph 1994, Randolph et al. 1998). The main motivations for their introduction included:

- Penetrometer shapes that were amenable to plastic limit analysis, with resistance independent of the pre-yield soil stiffness.
- Sufficient ratio of projected area to shaft area to render corrections for pore pressure effects and overburden stress minimal.
- Ability to measure remoulded penetration resistance directly, through cycles of penetration and extraction over a limited depth range.
- Reduced reliance on site-by-site correlations to obtain resistance factors, and hence shear strength profiles.

The last of these has proved something of a disappointment, not helped by an embedded culture with respect to interpretation of cone penetrometer data.

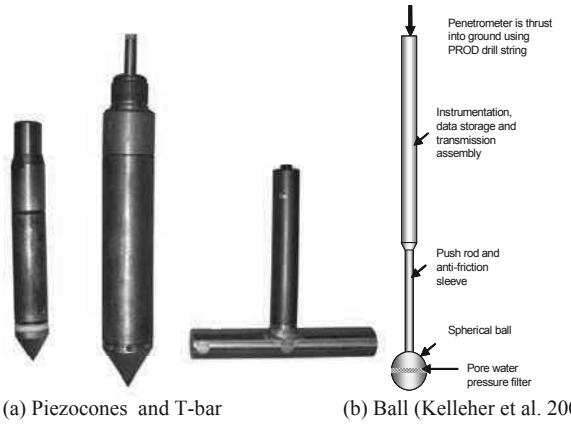

(a) Piezocones and T-bar (b) Ball (Kelleher et al. 2005)

Figure 10 Range of penetrometers for in situ testing.

The relatively large projected areas of 10,000 mm^2 for the standard T-bar, and generally 3000 to 5000 mm^2 for the ball penetrometers used offshore, makes them attractive for characterising soft clay deposits, but still with a capability to penetrate sand layers with cone resistance of up to 3 or 4 MPa. In particular, full-flow penetrometers have become the de facto standard for strength profiling in the upper few metres, with application to pipeline and riser design. Measurement of remoulded resistance from cyclic tests, which also help to constrain the accuracy of the monotonic penetration data, is essential for pipeline design. While both geometries are used, with the T-bar having superficial similarity to an element of pipe, the ball is a kinder geometry and has the advantage of enabling pore pressure measurement, as discussed later.

Plasticity solutions for the T-bar and ball in ideal (non-softening, rate independent) soil give resistance factors that may be approximated by Equation (13) or $N_{Tbar\text{-}ideal} = 9 + 3\alpha$, and

$$\frac{P_u}{0.25D^2 s_u} = N_{ball-ideal} \sim 11.21 + 5.04\alpha - 1.06\alpha^2 \qquad (25)$$

for the ball (Randolph et al. 2000, Einav and Randolph 2005). A close linear fit for the ball is $N_{ball\text{-}ideal} \sim 11.3 + 4\alpha$. Both sets of results are for a Tresca soil model, and lead to resistance factors for the ball that are 22 to 27 % greater than for the T-bar. This difference reduces using a von Mises strength criterion, for example down to about 15 % for an interface friction ratio of 0.3. Further reduction occurs for anisotropic shear strengths, with a difference of 7 % for a ratio of triaxial extension and compression strengths of 0.5 (Randolph 2000).

Experimental data are mixed in relation to any difference between T-bar and ball penetration resistance, with some reported profiles that are indistinguishable (Boylan et al. 2007, Low et al. 2011), whereas profiles in highly sensitive clays show differences of up to 16 %. This difference may be attributed partly to greater reduction in the T-bar resistance due to strain softening, compared with the ball (Einav and Randolph 2005). For soils of moderate sensitivity, the penetration resistances for T-bar and ball are mostly within 5 to 10 %, which is consistent with analytical results that take account of strength anisotropy.

In natural soils, as opposed to the idealised perfectly plastic, rate independent material on which plasticity solutions are based, it is essential to allow for the relatively high strain rates in the soil around the penetrometer, and also the gradual softening of the soil as it flows around the cylinder or ball. This has been looked at using a variety of numerical techniques, ranging from a combined upper bound and strain path method (UBSPM; Einav and Randolph 2005), large deformation finite element analysis (LDFE; Zhou and Randolph 2009a), and a steady state finite difference approach (SSFD; Klar and Pinkert 2010). All three approaches adopted a similar logarithmic law of rate dependence, with a relative strength gain of μ per tenfold increase in strain rate, and an exponential softening law with 95 % reduction to the fully remoulded shear strength for a cumulative plastic strain of ξ_{95}. Of the three approaches, the LDFE analysis tends to give the lowest (average) resistance, since it is able to capture the periodic generation and softening of distinct shear bands, accompanied by a corresponding cyclic variation in the penetration resistance.

Resistance factors evaluated using LDFE analysis (see Figure 11) may be expressed as (Zhou and Randolph 2009a)

$$N_{Tbar} \approx (1 + 4.8\mu)\left(\delta_{rem} + (1 - \delta_{rem})e^{-1.5\xi_{Tbar}/\xi_{95}}\right)N_{Tbar-ideal}$$
$$N_{ball} \approx (1 + 4.8\mu)\left(\delta_{rem} + (1 - \delta_{rem})e^{-1.5\xi_{ball}/\xi_{95}}\right)N_{ball-ideal} \qquad (26)$$

The quantity, ξ_{Tbar}, in Equation (26) reflects the average plastic shear strain experienced by a typical soil element as it flows around the T-bar. The corresponding quantity for a ball was found to be about 10 % lower ($\xi_{ball} \sim 3.3$, compared with $\xi_{Tbar} \sim 3.7$ – Zhou and Randolph 2009a). Of course, the actual degree of softening will vary with the original distance of the soil element from the axis of the advancing penetrometer, since soil elements immediately adjacent to the penetrometer will undergo the greatest softening.

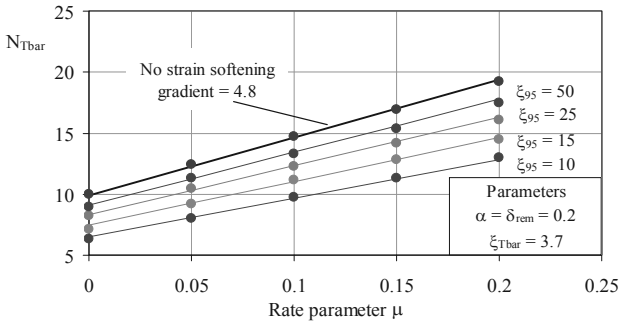

Figure 11 Values of T-bar resistance factor after allowing for rate effects and strain softening (sensitivity of $S_t = 5$, friction ratio, $\alpha = 0.2$).

The terms, $1 + 4.8\mu$, in Equation (26) reflect the average strain rate, which is some 5 orders of magnitude greater than the nominal 'laboratory' reference strain rate of 1 %/hr. This term should be viewed with some caution, owing to the limitations of the logarithmic rate law itself, and the inadvisability of trying to extrapolate over such a large range of strain rates.

Notwithstanding the above reservation, the analytically derived T-bar and ball factors carry information and should be made use of during the interpretation of field data. Where both ball and T-bar penetrometers are used (and similarly for cone and either T-bar or ball penetrometers), resistance factors should fall within an appropriate relative range, for example with N_{ball} no more than 10 % greater than N_{Tbar} unless the soil sensitivity exceeds 10.

Low et al. (2010) summarised penetrometer data from a number of offshore (and some onshore) sites around the world, recommending global average resistance factors of 11.9 (with standard deviation of 1.4) for T-bar and ball, relative to an average or laboratory simple shear strength. A similar value of 12 was proposed for N_{Tbar} for low sensitivity clays by DeJong et al. (2011), although their ball factor was 10 % higher. These values are plausible, in relation to Figure 11, for example for soils with a rate dependency factor of $\mu \sim 0.1$, sensitivity of 3 to 5 and ξ_{95} in the range 15 to 25.

Some of the parameters that determine the resistance factors can be deduced from the tests themselves; thus cyclic tests enable the sensitivity to be estimated, while tests at different penetration speeds (best performed at the end of a cyclic test when the soil strength has stabilised to the remoulded value) allow the rate parameter to be assessed. The resistance factors from individual sites summarised by Low et al. (2010) suggest that for soils of moderate plasticity the T-bar and ball resistance factors are closer to 11 than 12, while in the ultra-high plasticity soils off the coast of West Africa the average was around 13. This suggests higher strain rate dependency of the West African soils, for example with μ closer to 0.15 rather than 0.1.

Higher sensitivity implies low interface friction ratio, as well as greater loss of strength during passage of the penetrometer. Numerical analysis for rate dependent ($\mu = 0.1$) and softening ($\xi_{95} = 15$) material, gave ball resistance factors reducing from 21.5 to 11.6 for sensitivities increasing from 1 to 100 (Zhou and Randolph 2009b). Reducing these by the theoretical ratios for T-bar and ball resistances for Tresca soil leads to a relationship for T-bar resistance factors of:

$$N_{Tbar} \sim 9\left(1 + S_t^{-1}\right) \tag{27}$$

so ranging from a hypothetical 18 for non-softening soil, to a lower limit of 9 for ultra-high sensitivity. For typical sensitivities of offshore sediments in the range of, say, 3 to 10, the resulting resistance factors would lie between 12 and 9.9. Values above or below this range imply respectively higher or lower rate dependency, or sensitivities outside 3 to 10. The form of variation of resistance factor with soil sensitivity is quite similar to that observed experimentally by DeJong et al. (2011) for sensitivities up to about 10, beyond which the experimental resistance factors (based on field vane strength data) continued to fall, with a lower limit of around 6.

5.1 *Field measurement of consolidation coefficient*

The consolidation characteristics of seabed sediments determine the time scale of consolidation following foundation installation, or after cyclic loading that may have caused partial liquefaction. They also determine whether continuous motion, such as a penetrometer test or the axial and lateral movement of a pipeline during thermal buckling, occurs in a drained or undrained manner. It is therefore important to measure the consolidation coefficient, c_v, either from laboratory testing or from field dissipation tests following piezocone penetration.

Piezocone dissipation tests are commonly interpreted by fitting the excess pore pressure decay to the numerically determined consolidation solution of Teh and Houlsby (1991). This may be approximated (as in Equation (1)) as

$$U = \frac{\Delta u}{\Delta u_{ref}} \sim \frac{1}{1 + \left(T / T_{50}\right)^b} \tag{28}$$

where Δu_{ref} is the reference excess pore pressure that corresponds (ideally) to the initial excess pore pressure at the moment where the piezocone penetration ceases. Time t is normalised as $T = c_v t / d_{cone}^2$, and T_{50} is the normalised time for 50 % excess pore pressure dissipation. (The notation c_h is often used, rather than c_v, for the consolidation coefficient deduced from piezocone dissipation tests, to emphasise the primary direction of pore fluid flow.) As noted earlier, the exponent, b, is about 0.75, and T_{50} may be approximated as 0.061 times the square root of the rigidity index, I_r.

Determination of c_v in this way relies on the penetration phase to have occurred under undrained conditions, for which it is necessary know the consolidation coefficient! Some insight into this circular argument may be obtained by the simple assumption that pore pressure dissipation is a continuous process, some of which may occur during the penetration phase, and the rest of which continues, once the piezocone is halted, during the (subsequent) dissipation phase. This is a slight simplification, but it has proved useful in identifying limits on the reliability of interpreting dissipation tests (DeJong and Randolph 2012).

Excess pore pressure data from numerical analysis (e.g. Yi et al. 2012) and experiments (Randolph and Hope 2004, Schneider et al. 2007), where the piezocone was installed at different rates to span drained to undrained conditions, can be fitted by

$$\frac{\Delta u_{p0}}{\Delta u_{ref}} \sim \frac{1}{1 + \left(V / V_{50}\right)^c} \tag{29}$$

where Δu_{p0} is the excess pore pressure during the penetration, which in the field situation would become the initial excess pore pressure for a dissipation test. The normalised velocity, V, is defined as $V = v d_{cone} / c_v$, and V_{50} is the normalised velocity at which Δu_{p0} is 50 % of the reference 'undrained' excess pore

pressure, Δu_{ref}. Best fit parameters to the numerical and experimental data are $V_{50} \sim 3$, and the exponent $c \sim 1$.

Adopting Δu_{p0} as the initial excess pore pressure, falsely assuming undrained penetration, will lead to underestimation of the consolidation coefficient, because the time, t_{50}, for (a further) 50 % dissipation will be longer than if the penetration phase had indeed been undrained. Detailed analysis of this is provided by DeJong and Randolph (2012), and the resulting hypothesised relationships between t_{50} and c_v are illustrated in Figure 12, taking $I_r = 100$ and $V_{50} = 3$. An interesting feature of the results is that, for the best fit parameters of $b = 0.75$ and $c = 1$, the value of t_{50} reaches a minimum of about 10 s for $c_v \sim 400$ to 500 mm^2/s (around 15,000 m^2/yr), before starting to increase again. Obviously this contrasts with the monotonically decreasing relationship for true undrained conditions provided by the Teh and Houlsby (1991) solution.

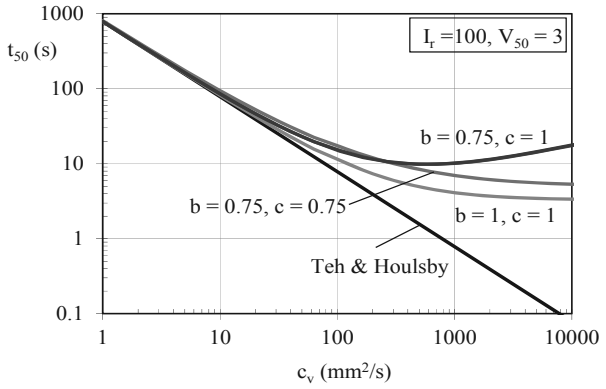

Figure 12 Variation in anticipated t_{50} with c_v, following partially drained penetration.

For the same values of V_{50}, b and c, and assuming standard piezocone parameters of $d_{cone} = 36$ mm and $v = 20$ mm/s, the relationship in Figure 12 may be written as (DeJong and Randolph 2012):

$$t_{50} \sim \frac{\sqrt{I_r}}{c_v}\left(78 + 0.25c_v^{1.2}\right) \qquad (30)$$

The corresponding minimum values of t_{50} range between 7 and 20 s, for rigidity index, I_r, between 50 and 400. From Figure 12, the standard interpretation of a piezocone test becomes questionable once t_{50} is less than about 50 s.

Ball penetrometers are also generally fitted with pore pressure sensors, in commercial practice either at the tip or at the 'equator' position (maximum diameter). However, experimental data has shown that, even in normally or lightly overconsolidated clay, the excess pore pressure tends to rise initially at the equator position at the start of a dissipation test, and the overall shape of the dissipation response varies somewhat between tests (DeJong et al. 2008). By contrast, pore pressure measurement at the 'mid-face' (a latitude of 45 º south from the equator) gives more consistent data, and with the maximum excess pore pressure occurring at the start of the dissipation test, provided the penetration occurs under undrained conditions (Mahmoodzadeh and Randolph 2013).

Typical dissipation responses from centrifuge model tests of piezocone and piezoball penetrometers in normally consolidated kaolin clay are shown in Figure 13. The time axis has been normalised by the diameters (10 mm for the cone, and 15 mm for the ball) and c_v values based on data from Rowe cell tests. For the relevant stress level of 110 kPa, the Rowe cell c_v is 4 m^2/yr. This has been multiplied by the λ/κ ratio of 4.7 for the Modified Cam Clay kaolin parameters adopted for the LDFE analyses, to reflect the (primarily) swelling stress path during pore pressure dissipation, giving $c_v = 19$ m^2/yr (0.6 mm^2/s).

The piezocone experimental data match reasonably well the Teh and Houlsby (1991) solution for rigidity index of $I_r = 76$ (consistent with the model for kaolin adopted in numerical analysis). The experimental piezoball data are compared with a dissipation curve obtained by large deformation finite element (LDFE) analysis using the Modified Cam Clay model and a permeability consistent with the Rowe cell c_v value (Mahmoodzadeh et al. 2013). Both theoretical and experimental dissipation curves show a difference in T_{50} by a factor of 5, compared with the factor of ~2.5 observed by Low et al. (2007) from field tests using a piezoball with pore pressure sensor at the equator.

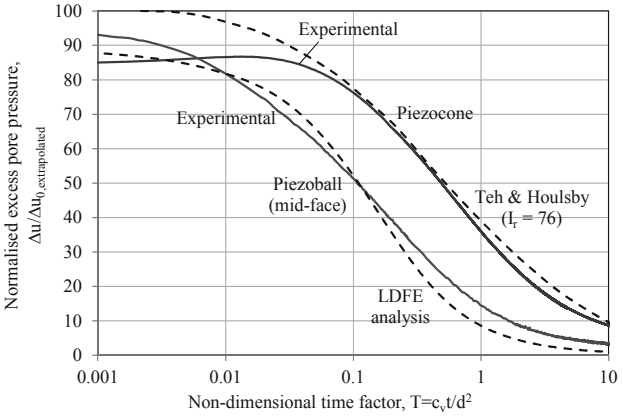

Figure 13 Dissipation responses from centrifuge model piezocone and piezoball tests compared with numerically derived dissipation curves.

One of the primary design applications requiring knowledge of the consolidation coefficient is for pipeline design, where the focus is on the upper 0.5 m or so of the seabed. It would be difficult to obtain meaningful data from dissipation testing within that zone, since the proximity to the free surface would affect both the initial stress field following penetration, and potentially the drainage paths and thus the dissipation response. An alternative approach has been proposed recently, which also minimises any time penalty associated with the duration of conventional dissipation testing. The proposed device is a 'parkable' piezoprobe, as shown schematically in Figure 14 (Chatterjee et al. 2013). It comprises a solid steel cylinder with hemispherical ends, approximately 250 mm in diameter and 375 mm high. An outrigger may be fitted to provide sufficient force (of 1 to 2 kN) and to limit the embedment to no more than one diameter. The device is designed to be lowered by a winch, from either an ROV or a seabed site investigation system, with measurements gathered in parallel with the main site investigation activities, thus minimising time penalty.

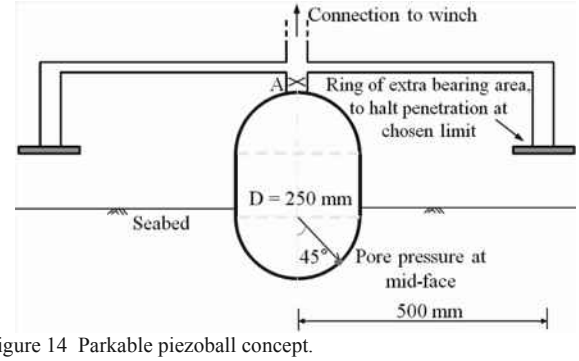

Figure 14 Parkable piezoball concept.

In order to provide a theoretical framework to validate the design concept and establish appropriate dissipation curves, LDFE analyses were undertaken. Figure 15 shows contours of

initial excess pore pressure, normalised by the invert value, for two different boundary conditions (Chatterjee et al. 2013). Natural conditions (left side) with the shear strength increasing linearly with depth were simulated using a nominal 1 kPa surcharge at mudline (the minimum to allow numerical stability during the analysis). Alternatively, in order to simulate approximately uniform strength and stiffness conditions, an artificial 200 kPa surcharge was applied (right side).

The resulting consolidation responses are shown in normalised form in Figure 16 for two different embedments (w/D = 0.5 and 1). For comparison, dissipation curves for a pipeline (two-dimensional) and a deeply embedded piezocone (Teh and Houlsby solution) are also shown. The parkable pieozoprobe (PPP) shows more rapid dissipation, for a given diameter, due to its geometry and shallow embedment. For comparison, a curve for a standard diameter piezocone is also shown, scaled according to the relevant diameters. Although the PPP takes longer for the excess pore pressures to dissipate (by a factor of about 7 for t_{50}), the concept for the device is that this occurs in parallel with the primary site investigation activities, so off the critical time line.

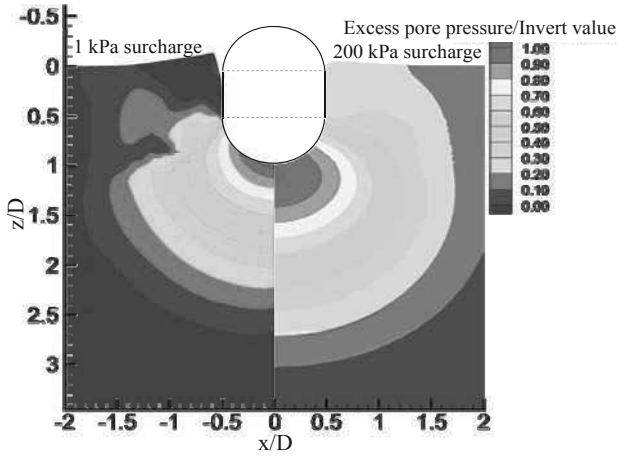

Figure 15 Initial normalised excess pore pressure distributions for cases of strength increasingly linearly with depth (1 kPa surcharge) and quasi-homogenous conditions (200 kPa surcharge).

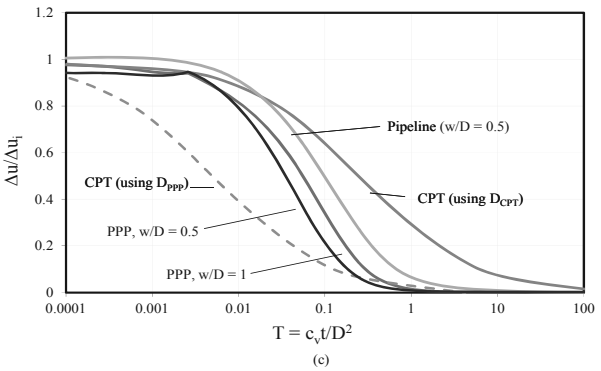

Figure 16 Pore pressure dissipation time history for different geometries and embedment (after Chatterjee et al. 2013).

6 PIPELINES AND RISERS

Geotechnical engineering design for pipelines and risers has matured significantly over the last decade, responding to the buckling related design challenges arising from thermal and pressure-induced expansion and contraction of deep water pipelines. (Note, the terminology 'pipelines' is used here generically, to include the many different functional names used in the industry, covering flowlines, umbilicals, MEG lines and export pipelines.) Summaries of recent developments have been provided in the keynote papers of Cathie et al. (2005) and White and Cathie (2010). Here, a brief overview is given of some analytical results that have contributed to design approaches.

In deep water, geotechnical design is concerned primarily with issues associated with lateral buckling, which has been the topic of a longstanding joint industry project, the SAFEBUCK JIP (Bruton et al. 2007, 2008). Pipeline buckling is engineered, rather than suppressed, by appropriately spaced buckle initiators, or snake-lay of the pipeline. The axial and lateral resistance offered by the shallow sediments on which the pipelines rest are key inputs to the design. Both of these depend firstly on the embedment of the pipeline into the sediments, and secondly on the velocity and time scale of the movement relative to the soil consolidation characteristics.

6.1 *Pipeline embedment*

Pipeline embedment occurs during the lay process, while the pipeline is suspended from the lay vessel, in much the same way as a (more permanent) steel catenary riser (SCR) is suspended from a floating production system (Figure 17). Embedment occurs due to the submerged weight of the pipeline, which is augmented by static and dynamic force concentrations for each segment of pipeline as it passes through the touchdown zone. The period within the touchdown zone, and hence the extent of cyclic motions undergone by a given segment of pipe due to wave-induced motions of the lay vessel, will depend on the lay rate; the magnitude of the motions and ratio of dynamic to static force concentration will depend on the sea state conditions as the pipeline is laid.

At intermediate depth scales the shear strength profile of deep water sediments may show a mudline intercept of a few kPa (Colliat et al. 2010). However, in the upper 0.5 m that is critical for pipeline design, there is rarely any detectable strength intercept at the mudline. The initial shear strength gradient, ρ, may range from as low as 1 to 1.5 kPa/m, where there is no crustal feature, to ~30 kPa/m, where locally high shear strengths occur, typically at depths of 0.4 to 1 m. Such crustal features are considered to be due to bioturbation (DeJong et al. 2013, Kuo and Bolton 2013).

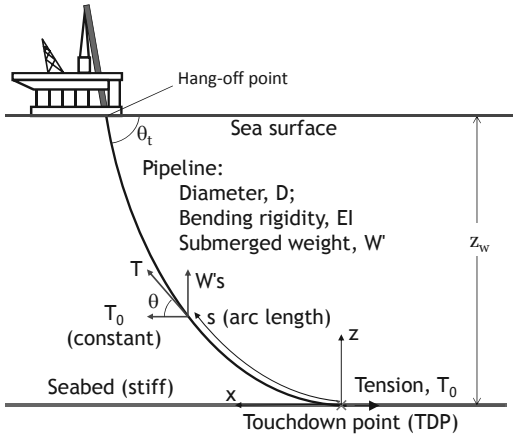

Figure 17 Schematic of SCR or pipeline during lay process.

The static penetration resistance for a pipeline of diameter, D, in sediments with strength proportional to depth may be expressed as (Chatterjee et al. 2012a)

$$\frac{V}{\rho D^2} = 4.7\left(\frac{w}{D}\right)^{0.17} \qquad (31)$$

where ρ is the shear strength gradient and V and w are the vertical force per unit length and penetration respectively.

Within the range of interest (w/D ~ 0.2 to 0.5), this may be approximated by a linear 'plastic' spring of stiffness

$$k_{vp} = \frac{V}{w} \sim 4\rho D \quad (32)$$

In addition to the 'geotechnical resistance' given by the above relationships, allowance must be made for buoyancy effects as the pipeline becomes embedded within the soil (Merifield et al. 2009). This adds a component of resistance that effectively increases the shear strength gradient by a factor that is of the order of $1 + f\gamma'/\rho$, with f ~ 0.15 to 0.25 depending on the embedment and amount of heave adjacent to the pipeline. Under dynamic lay conditions, lateral motion of the pipe will tend to reduce the amount of soil heave adjacent to the pipe.

The linear penetration stiffness allows the complete response of the pipeline (or SCR) to be determined through the touchdown zone, using analytical solutions based on a boundary layer approach (Lenci and Callegari 2005, Palmer 2008, Yuan et al. 2012). A characteristic length, λ, reflecting the length of the touchdown zone, emerges from the solutions and is given by

$$\lambda = \sqrt{\frac{EI}{T_0}} \quad (33)$$

where EI is the bending rigidity of the pipe and T_0 the horizontal component of tension in the catenary (Figure 17). The effect of the seabed stiffness, k_{vp}, on the profile of contact force, V, through the touchdown zone is shown in Figure 18.

The maximum static contact force, V_{max}, normalised by the submerged weight of the pipe, W', is a function of the seabed stiffness, and also of the characteristic length, λ, as shown in Figure 19. The variation of V_{max} may be approximated as (Randolph and White 2008a)

$$\frac{V_{max}}{W'} \sim 0.6 + 0.4\left(\lambda^2 k_{vp} / T_0\right)^{0.25} \quad (34)$$

A typical range for V_{max}/W' for deep water pipelines is 1.5 to 3, as indicated in Figure 18.

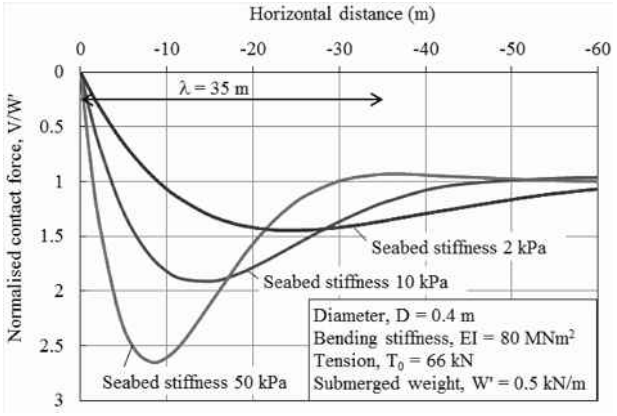

Figure 18 Profiles of normalised contact force for different values of seabed stiffness.

Westgate et al. (2012) suggested that, as a first approximation, pipeline embedment under typical lay conditions may be estimated based on the maximum static contact force, V_{max}, and assuming fully remoulded shear strength for the soil. Combining Equations (32) and (34), but with the shear strength gradient, ρ, replaced by the remoulded strength gradient, $\rho_{rem} = \rho/S_t$, then gives

$$\frac{w}{D} \sim \frac{1 + \left(\lambda^2 \rho_{rem} D / T_0\right)^{0.25}}{7\rho_{rem} D^2} W' \quad (35)$$

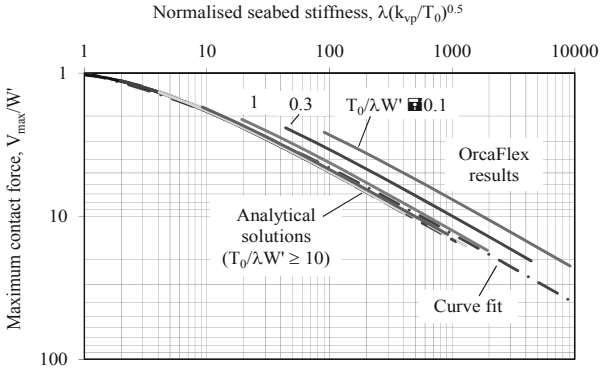

Figure 19 Maximum static contact force in touchdown zone (Randolph and White 2008a).

Effects of buoyancy may be incorporated by adjusting W' iteratively, or by factoring the remoulded strength gradient by $1 + f\gamma'/\rho_{rem}$, taking f in the range 0.15 to 0.25.

The simple approach of using the remoulded shear strength balances two compensating factors. On the one hand assumption of fully remoulded conditions exaggerates the actual degree of softening under typical lay conditions. This is balanced by using the maximum static force, V_{max}, to estimate embedment, rather than the maximum dynamic force, V_{dyn}, which is typically 25 to 50 % greater than V_{max} but can be even larger in more severe sea states (Westgate et al. 2010).

A more refined treatment of pipeline embedment was described by Westgate et al. (2013), taking account of:

- The estimated number of motion cycles experienced by each section of pipeline as it passes through the touchdown zone.
- Combined horizontal and vertical motions.
- Gradual softening of the soil resulting from cumulative displacement of the pipeline relative to the soil due to the cyclic motions.

The approach builds on the model for cyclic degradation of the resistance of full-flow penetrometers during penetration and extraction cycles (Zhou and Randolph 2009b), but incorporating a brittle 'structured' component of soil strength that is lost rapidly (Randolph et al. 2007). The effect of horizontal motion is incorporated by considering theoretical yield envelopes in V-H space, from which an associated flow rule allows estimation of the ratio of vertical to horizontal movements (Cheuk and White 2011).

Although built on reasonable theory, the model incorporates empirical adjustment factors, which were calibrated through centrifuge model tests. The model was then applied to three sites where field data were available from post-installation surveys, in addition to video footage during the lay process that allowed estimation of the amplitude of horizontal pipe motions. The observed pipeline embedment was found to lie within the range predicted for 'light', 'moderate' and 'severe' sea states (Figure 20).

Direct application of Equation (35), factoring the remoulded shear strength gradient, leads to estimated embedment, w/D, in the range 0.28 to 0.33, which is consistent with the most frequently observed values. However, it is evident from Figure 20, and other field cases reported by Westgate et al. (2013), that the pipeline embedment should be considered as a non-deterministic quantity, varying with lay conditions even if the seabed properties are relatively uniform along the pipeline route. This is consistent with modern probabilistic design approaches for pipelines (White and Cathie 2010). The detailed treatment for estimating pipeline embedment proposed by Westgate et al. (2013) allows probabilistic distributions of pipeline embedment to be derived in a logical manner.

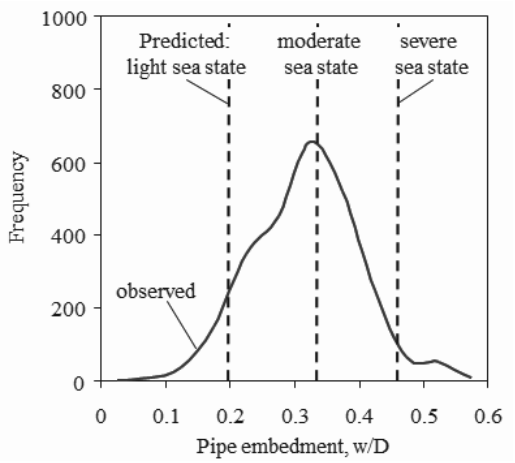

Figure 20 Comparison of predicted and observed pipeline embedment (from Westgate et al. 2013, Site C).

6.2 *Lateral resistance*

The lateral resistance of partially embedded pipelines may be assessed, as for shallow foundations, from failure surfaces in vertical (V) – horizontal (H) load space. The form and size of failure envelope depend on factors such as the embedment, the pipe-soil interface condition (friction ratio, α, ranging between 0 for smooth to 1 for rough; and whether tensile stresses are permitted), the shear strength profile (ranging from uniform to varying proportionally with depth) and the relative magnitudes of effective stress and shear strength.

Theoretical failure envelopes considering some or all of these variables have been presented by Randolph and White (2008b: analytical upper bound solutions), Merifield et al. (2008: finite element analyses) and Martin and White (2012: closely bracketed finite element based lower and upper bound plasticity solutions). An example from the most recent of these is shown in Figure 21, for a fully rough pipeline embedded in soil with strength proportional to depth, for two different ratios of effective stress to shear strength gradient (γ'/ρ).

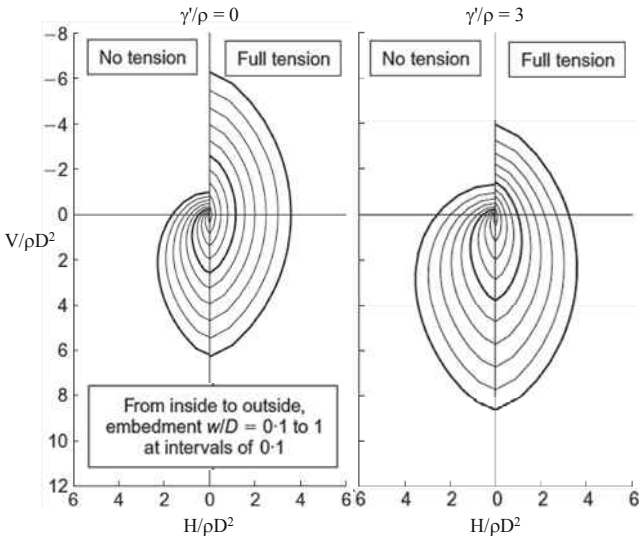

Figure 21 Examples of failure envelopes for rough pipelines in soil with strength proportional to depth (Martin and White 2012).

There is a significant difference in lateral and uplift resistance depending on the assumption of full tension or no tension at the pipeline surface. The slight uplift resistance for the case of no tension is primarily due to soil above the pipeline for embedment ratios exceeding 0.5. In practice, model test data indicate that, during lateral displacement, the tensile resistance on the trailing edge of a pipeline is extremely brittle, so that the relevant failure envelope reverts quickly to that for no tension.

The theoretical failure envelopes referred to above are based on ideal, rate independent non-softening soil, and ignore any local heave (relative to the flat seabed) adjacent to the pipeline. A more realistic study, based on LDFE analysis, that takes account of such features was presented by Chatterjee et al. (2012b). For the particular set of soil parameters investigated, they derived failure envelopes that were approximately parabolic, expressed as

$$\beta\frac{H_{max}}{V_{max}}\left(\frac{V}{V_{max}}\right)^{\beta_1}\left(1-\frac{V}{V_{max}}\right)^{\beta_2}-\frac{H}{V_{max}}=0 \qquad (36)$$

$$\text{where } \beta=\frac{(\beta_1+\beta_2)^{\beta_1+\beta_2}}{\beta_1^{\beta_1}\beta_2^{\beta_2}}$$

The quantities β_1, β_2 and H_{max}/V_{max} were found to vary with embedment according to

$$\beta_1 = 0.59 + 0.89\, w/D$$
$$\beta_2 = 0.55 + 0.87\, w/D \qquad (37)$$
$$H_{max}/V_{max} = 0.17 + 0.31\, w/D$$

The failure envelopes allow estimation of the breakout lateral resistance for any given vertical load ratio, V/V_{max}, and loading path. As a pipeline is displaced laterally it tends to rise towards the seabed, or plunge deeper, depending on the initial embedment and vertical load ratio. After sufficient movement it will reach a steady residual horizontal resistance, H_{res}. Pipeline trajectories during breakout, and a methodology for assessing the residual resistance ratio, H_{res}/V, were also presented by Chatterjee et al. (2012b).

6.3 *Axial resistance*

The axial resistance of pipelines is an intriguing problem that, at face value, would seem to be essentially trivial (a sliding failure with known vertical load), but in practice turns out to be more complex. There are three main aspects that need to be considered (Hill et al. 2012):

- The pipe-soil interface friction, which is affected by the relative roughness of the pipeline coating, and also the magnitude of the normal effective stress. At the very low effective stresses (generally less than 5 kPa) applied by deep water pipelines, the effective stress failure envelope shows significant curvature.
- The cylindrical geometry of the pipeline, which for any given embedment leads to integrated normal effective stresses around the pipe-soil interface that exceed the pipeline weight by a so-called 'wedging factor'.
- Excess pore pressure development at the pipe-soil interface, which leads to a strong dependence of the axial resistance on the velocity and cumulative axial displacement.

The first of these requires appropriate experimental data, typically obtained using direct shear devices that have been adapted for very low normal stresses. Analytical solutions can provide a theoretical basis for the other aspects, and these are discussed here.

The basis for estimating the wedging factor, ζ, due to the cylindrical pipe surface is illustrated in Figure 22. Drawing on the classical solution for the stresses due to a line load acting on the surface of a homogeneous elastic half-space, a $\cos\theta$ variation of the normal effective stress may be assumed (with the magnitude of the induced 'radial' stresses decaying inversely with radius from the pipe centre). Integrating the

normal effective stresses around the perimeter, P, of the interface, with S adjusted to balance the submerged pipeline weight, W', allows the average normal effective stress, q, to be expressed as

$$q = \zeta \frac{W'}{P} \quad \text{with} \quad \zeta = \frac{2\sin\theta_m}{\theta_m + \sin\theta_m \cos\theta_m} \le 1.27 \qquad (38)$$

$$\text{and} \quad P = D\theta_m \le \pi D/2$$

The value of θ_m is related to the normalised embedment by $\cos\theta_m = 1 - 2w/D$.

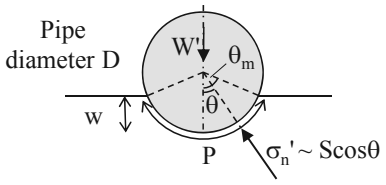

Figure 22 Schematic of embedded pipe.

Within a conventional critical state framework, the effect of the time scale for axial movement may be evaluated by considering the tendency for the adjacent soil to compact, or dilate, and the resulting maximum (in an absolute sense) excess pore pressure that may develop during rapid shearing. This is illustrated in Figure 23 for the case of contractive soil. The potential maximum reduction in void ratio, $-\Delta e_{max}$, during drained shearing is equivalent to a state parameter (Been and Jefferies 1985), although more usefully expressed in terms of volumetric strain, $\Delta\varepsilon_{v,max}$. The corresponding maximum excess pore pressure during undrained shearing is then obtained from

$$\ln\left(1 - \frac{\Delta u_{max}}{q}\right) = \frac{\Delta e_{max}}{\lambda} = -\frac{1+e_0}{\lambda}\Delta\varepsilon_{v,max} = -\frac{\Delta\varepsilon_{v,max}}{\lambda^*} \qquad (39)$$

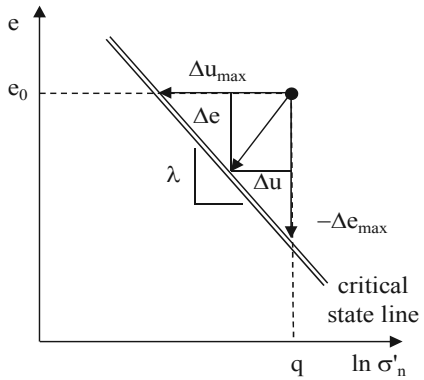

Figure 23 Critical state framework for stress paths during shearing.

The proportion of Δu_{max} that develops at the pipeline-soil interface depends on the velocity and time scale (or cumulative displacement) of the axial motion. For slow movement, excess pore pressure can dissipate as fast as it is generated, and the response is fully drained, while at the opposite extreme high excess pore pressures are generated initially, although should dissipate with continued displacement.

An example response is shown in Figure 24 from FE analysis of a pipeline resting on normally consolidated Modified Cam Clay, with a plane strain friction angle of 27 º (Randolph et al. 2012). The theoretical wedging factor for w/D = 0.4 is 1.25, so that the drained axial friction factor is F/W' ~ 1.25tan(27) = 0.64. For fast shearing the initial excess pore pressure ratio, $\Delta u_{max}/q$, is about 0.45, so that the undrained friction ratio is (1 – 0.45)×0.64 = 0.35.

With increasing elapsed time, or displacement (noting that $c_v t/D^2$ is equivalent to $(\delta/D)/(vD/c_v)$), the excess pore pressures dissipate and the friction ratio increases to the drained value. The form of the backbone curve that quantifies the degree of consolidation as a function of $T = c_v t/D^2$ may be approximated as (Randolph et al. 2012):

$$\frac{F}{W'} = \left(\frac{F}{W'}\right)_d - \left[\left(\frac{F}{W'}\right)_d - \left(\frac{F}{W'}\right)_u\right] e^{-\ln(2)(T/T_{50})^m} \qquad (40)$$

where the subscripts d and u denote drained and undrained limits, m ~ 0.5 and T_{50}, representing the non-dimensional time where the friction ratio is midway between drained and undrained limits, is about 0.05.

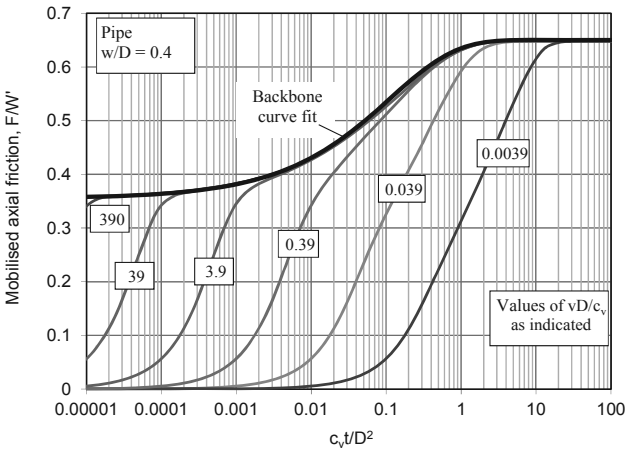

Figure 24 Example axial response of pipeline as a function of non-dimensional time and velocity.

Unfortunately, data from extensive model tests on pipe segments are not consistent with the theoretical framework of critical state soil mechanics and consolidation described above. The data show that excess pore pressures may be regenerated during fast axial motion that follows slow, drained, axial displacement, and indeed the axial friction has generally been considered as a function of the shearing velocity rather than the elapsed time during a given motion (White et al. 2011).

A model that broadly reproduces the trends observed in the model tests was suggested by Randolph et al. (2012). The model supposes that pore pressure is continuously generated during shearing, in response to volumetric collapse (generically referred to as 'damage') within the soil adjacent to the pipe. The rate of (potential) volumetric strain was assumed proportional to the shear strain rate (denoted by normalised velocity, v/D) and to the current normal effective stress, so that no further damage would occur if the effective stress were to fall to zero. Taking the rate of volumetric collapse (or damage) as $\alpha v/D$, the rate of excess pore pressure generation becomes

$$\frac{du/dt}{q} = \frac{\alpha}{\lambda^*}\frac{v}{D}\left(1 - \frac{\Delta u}{q}\right) \qquad (41)$$

At high rates of shearing, the effect of damage is partially compensated by slight enhancement of the effective friction ratio due to increased shear strain rates. This may be modelled using standard models for rate dependency of shear strength, for example a form of Herschel-Bulkley relationship, so that the failure shear stress ratio becomes

$$\frac{\tau_f}{q} = \mu_{HB}\left(1 - \frac{\Delta u}{q}\right) = \mu_y\left(1 - \frac{\Delta u}{q}\right)\left[1 + \eta\left(\frac{v/D}{v_{ref}/D}\right)^{\beta}\right] \qquad (42)$$

where μ_y is the minimum (yield) friction coefficient at very slow shearing rates and η and β are the rate parameters; these combine to give the rate-enhanced friction coefficient, μ_{HB}.

Using the backbone consolidation curve shown in Figure 24 (Equation (40)) as the basis for pore pressure dissipation, the excess pore pressure may be obtained by a convolution integral of the form

$$\Delta u = \int_{t'=0}^{t} \frac{\alpha}{\lambda^*} \frac{v(t')}{D} \left(q - \Delta u(t')\right) e^{-\ln 2\left((T-T')/T_{50}\right)^m} dt' \qquad (43)$$

where v and Δu are both time varying functions and $T' = c_v t'/D^2$.

An example response is shown in Figure 25. Of particular note is that after an initial transient stage, the normalised friction, τ/q, converges to a steady value that is a function of velocity. At steady state, pore pressure generation due to damage balances pore pressure dissipation due to consolidation. The steady state friction was approximated as

$$\frac{\tau_{steady\ state}}{q} = \mu_{HB}\left(1 - \frac{1}{1 + 0.24/\left[(\alpha/\lambda^*)T_{50} vD/c_v\right]}\right) \qquad (44)$$

Although this model of velocity and time-dependent axial friction contains some speculative elements, such as the proposed link between pore pressure generation and normalised velocity, it provides a theoretical framework for design, and for the planning of future model tests in the laboratory or field. It also helps to resolve the apparent discrepancy between conventional consolidation theory and experimental data.

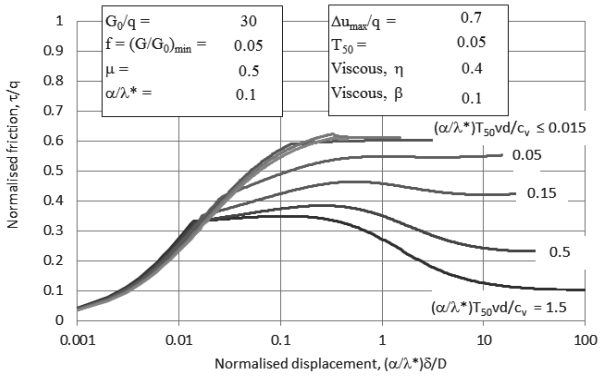

Figure 25 Example axial response of pipeline incorporating damage and strain rate (Randolph et al. 2012).

Axial stiffness

In addition to evaluating the limiting pipe-soil friction ratio, the pre-failure axial stiffness of the pipeline is important as a boundary condition for analysis of pipeline walking or the feed-in to lateral buckles or debris flow impact. At an element level, the axial stiffness (ratio of load transfer per unit length to axial displacement) may be estimated by assuming a simple distribution of shear stress around the perimeter of the pile, similar to that for normal effective stress (Figure 22).

Consider a pipeline that is embedded to w/D = 0.5, and where the shear stress resisting axial movement varies as $\cos\theta$ around the embedded section of the pipe. The shear stress will also decrease inversely with radius from the pipe axis, in order to satisfy equilibrium. Now assume a shear modulus for the soil that varies proportionally with depth, z, according to G = mz. At any radial position, the shear strain will therefore be

$$\gamma = \frac{\tau}{G} = \frac{\tau_{inv} D \cos\theta}{2r^2 m \cos\theta} = \frac{\tau_{inv} D}{2r^2 m} \qquad (45)$$

where τ_{inv} is the shear stress at the pipe invert. Integrating this with respect to r leads to the displacement at the pipe. The resulting axial load transfer stiffness is then given by

$$k_a = mD \qquad (46)$$

For a partially embedded pipeline, this may be reduced by a factor $\sin\theta_m$, where θ_m is defined in Figure 22. By comparison, the vertical stiffness for a (surface) foundation of width $D\sin\theta_m$ on similar soil would be given by $k_v = 2mD\sin\theta_m$ (Gibson 1974). Hence the axial stiffness is about half the vertical stiffness (a little lower, allowing for the embedded nature of the pipeline, Guha 2013).

The axial load transfer stiffness may be combined with the expression for the stiffness of a long pile (Equation (8)) in order to yield the overall pipeline stiffness for axial motion:

$$K_{pipe,axial} = \sqrt{(EA)_{pipe} k_a} = \sqrt{(EA)_{pipe} mD} \qquad (47)$$

6.4 *Impact forces from debris flows*

Geohazard assessment, particularly from submarine landslides, is a major aspect of developments in deep water, i.e. beyond the continental shelf, where relic landslides are frequently observed. While it is generally possible to site well manifolds and anchoring systems away from the flow paths of potential landslides, pipelines (particularly export pipelines) by their nature must frequently be exposed to some risk. It is therefore necessary to consider the magnitude of impact forces from debris flows, and also the resulting response of a pipeline in order to gauge whether it would survive impact.

The problem to be considered is shown schematically in Figure 26. The debris flow may be idealised as extending over a finite width, B, within which it imparts a normal force (per unit length), F_n, and an axial force, F_a. Outside the impact zone, passive lateral and axial resistance is provided between the pipeline and the soil.

Generic analytical solutions have been developed for the pipe response for given non-dimensional ratios of active loading to passive resistance, allowing estimates of the maximum stresses induced in the pipeline and maximum deflection under the action of the debris flow (Randolph et al. 2010). However, methods to estimate the loading itself have tended to lack a sound fundamental basis, being couched in terms of drag factors for normal and parallel components of flow. These lead to resistances that are functions of density and velocity of flow, rather than parameters linked to shear strength or even viscosity.

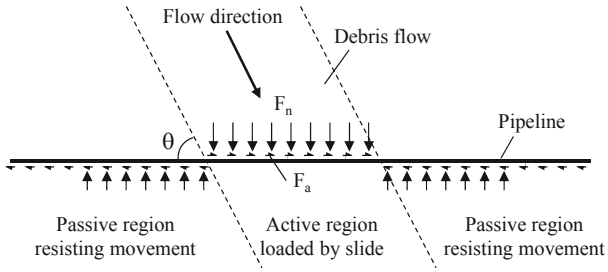

Figure 26 Schematic of debris flow impacting pipeline (Randolph and White 2012).

For flow normal to the pipeline ($\theta = 90°$ in Figure 26) a hybrid approach, combining 'geotechnical' and 'fluid drag' components of resistance, was proposed by Randolph and White (2012). The normal force per unit length of pipe, F_n, is expressed as

$$\frac{F_n}{D} = N_p s_{u,op} + C_d\left(\frac{1}{2}\rho v_n^2\right) \quad (48)$$

where N_p is a bearing factor, $s_{u,op}$ is the operative shear strength at a shear strain rate that reflects the (normal component of) flow velocity, v_n, and C_d is a drag coefficient. The relationship was calibrated against numerical analysis data (Zakeri 2009), and yielded drag coefficients in the range 0.6 to1.2 for flow angles between 30 and 90 º.

The principle behind Equation (48) is that the bearing factor, N_p, in common with other bearing factors in geotechnics, captures the geometry of the failure mechanism, and should be independent of velocity or soil strength, essentially as specified in Equation (13) but with adjustment for the relative depth of the debris flow compared with the pipeline diameter. The effect of velocity, or shear strain rate, is incorporated into the operative shear strength, using conventional relationships such as the Herschel-Bulkley expression in Equation (42), or a simple power law relationship:

$$s_{u,op} = s_{u,ref}\left(\frac{\dot{\gamma}}{\dot{\gamma}_{ref}}\right)^{\beta} \sim s_{u,ref}\left(\frac{v_n / D}{\dot{\gamma}_{ref}}\right)^{\beta} \quad (49)$$

The relative magnitudes of the two components in Equation (48) are such that the fluid drag term only becomes significant once the Johnson number (also referred to as the non-Newtonian Reynolds number), $\rho v_n^2/s_{u,op}$ exceeds about 5. The accuracy of this approach has recently been demonstrated through experimental work (Sahdi et al. 2013), where a drag factor of around 1.1 to 1.4 was suggested. Numerical analyses using the material point method (Ma, private communication) has confirmed a drag factor close to unity.

For flow parallel to the pipeline, analytical relationships have been derived for material that follows a power law function, as in Equation (49) (Einav and Randolph, 2006). The axial force per unit length, F_a, is given by

$$F_a = f_a s_{u,op} \pi D \quad \text{where } f_a = \left[2\left(\frac{1}{\beta} - 1\right)\right]^{\beta} \quad (50)$$

The value of f_a lies in the range 1.2 to 1.4 for typical values of β between 0.05 and 0.15.

For the general case of debris flow impacting a pipeline at an angle θ, a failure envelope may be developed to quantify the interaction between parallel and normal components of force. Based on the numerical data from Zakeri (2009), a failure envelope of the form

$$\left(\frac{f_a}{f_{a,0}}\right)^3 + \left(\frac{N_p}{N_{p,90}}\right)^1 = 1 \quad \text{with } N_p = N_{p,90}(\sin\theta)^{0.7} \quad (51)$$

was found to give a reasonable fit (Randolph and White 2012). An example failure envelope, taking $f_{a,0} = 1.4$ and $N_{p,90} = 11.9$ as appropriate for a rough pipe, is shown in Figure 27, together with spot points for flow angles of 0, 30, 45, 60 and 90 º.

Assessment of pipeline response to debris flow impact requires initial estimation of debris flow velocity, height (which affects N_p), relative angle and shear strength at the point of impact. These are non-trivial quantities to estimate, but may be gleaned from numerical modelling of landslide runout. The resulting impact forces and pipeline response may then be evaluated using the relationships summarised here.

An important consideration is that the normal velocity, v_n, used to determine the strain rate (hence operative shear strength) and the drag force should be the *relative* velocity between debris flow and pipeline. Initially, as the debris flow strikes the pipeline, it will carry the pipe with it. Resisting bending moments and axial tension in the pipeline will develop quite gradually as the pipeline is deformed. These will slow the pipeline, relative to the debris flow, until a dynamic equilibrium is established (Boylan and White 2013).

A single set of results from Randolph et al. (2010) is shown in Figure 28, for a case where the passive horizontal resistance of the pipeline outside the slide zone is half the active force, F_n, and the passive axial resistance is 25 % of F_n. The total active loading, F_n times the slide zone width B, is normalised by the pipeline cross-sectional rigidity, EA. The strains in the pipe become dominated by axial tension as the width of the debris flow increases; it is evident that relatively low levels of active loading can cause significant strains, and potentially failure of the pipeline.

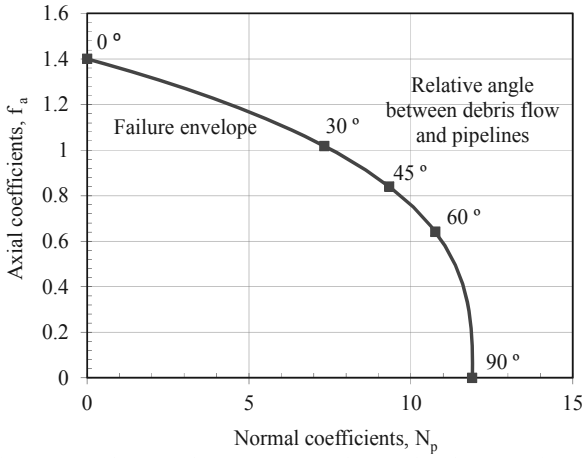

Figure 27 Failure envelope for varying flow angle relative to pipe axis (Randolph and White 2012).

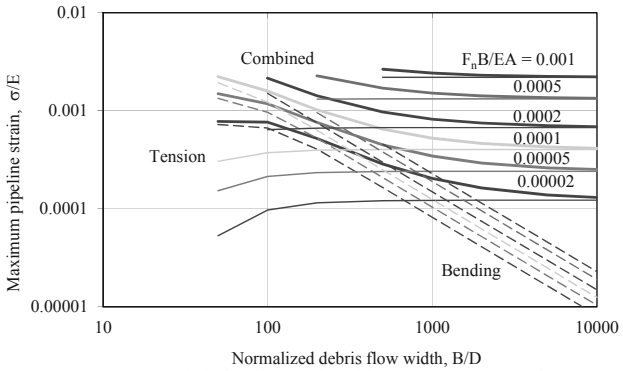

Figure 28 Effect of slide loading and width on maximum pipeline strain (Randolph et al. 2010).

7 CONCLUSIONS

Analysis underpins and enriches design approaches that we use in day to day practice. Where empirical correlations are still relied upon, we should strive continuously to understand the underlying processes and gradually capture them quantitatively through analysis or synthesis of well-considered numerical studies. The paper has dipped into a number of different application areas in offshore geotechnical design, with the aim throughout being to present simplified outcomes, based on analysis, that can be applied directly in design. It should be emphasised, however, that simplifications and idealisations in analytical solutions are such that final validation and fine-tuning of a design will often require further input from physical or numerical modelling of the specific application. Even there though, analytical solutions should guide the planning of the more sophisticated investigations.

Perhaps most importantly, analytical solutions are the clearest language through which engineering systems educate us in respect of the controlling behaviour in offshore geotechnical design. Simple relationships indicate which parameters we should pay close attention to and which parameters have less influence. In the early stages of a project, analytical solutions can highlight the parameters that are most important when targeting site investigations, and which aspects of our design offer the most scope for optimising performance.

8 ACKNOWLEDGEMENTS

The work reported here is underpinned by the activities of the Centre for Offshore Foundation Systems (COFS), currently supported as a node of the Australian Research Council Centre of Excellence for Geotechnical Science and Engineering, and in partnership with The Lloyd's Register Educational Trust. Support through the Australian Research Council's Discovery Program is also acknowledged. However, the most important acknowledgement is for the many colleagues in COFS, Advanced Geomechanics, and elsewhere who have contributed to specific results and any useful ideas presented here.

9 REFERENCES

Andersen, K.H. 2009. Bearing capacity under cyclic loading – offshore along the coast and on land. 21st Bjerrum Lecture. *Canadian Geotech. J.* 46, 513–535.

API 2011. *Recommended Practice 2GEO: Geotechnical and foundation design considerations, 1st Edition*. American Petroleum Institute, Washington.

Aubeny, C.P. and Chi, C. 2010. Mechanics of drag embedment anchors in a soft seabed. *J. Geotech. Geoenviron. Eng.,* ASCE, 136(1), 57–68.

Aubeny, C.P., Kim, B.M., and Murff, J.D. 2005. Proposed upper bound analysis for drag embedment anchors. *Proc. Int. Symp. on Frontiers in Offshore Geotechnics, ISFOG*, Perth, 179-184.

Aubeny, C.P., Kim, B.M. and Murff, J.D. 2008. Prediction of anchor trajectory during drag embedment in soft clay. *Int. J. Offshore Polar Eng.* 18(4), 314–319.

Baguelin, F., Frank, R. and Said, Y.H. 1977. Theoretical study of lateral reaction mechanism of piles. *Géotechnique* 27(3), 405-434.

Been, K. and Jefferies, M.G. 1985. A state parameter for sands. *Géotechnique* 35(2), 99-112.

Boylan, N., Long, M., Ward, D., Barwise, A. and Georgious, B. 2007. Full flow penetrometer testing in Bothkennar clay. *Proc. 6th Int. Conf. Offshore Site Investigation and Geotechnics*, Soc. for Underwater Technology, London, 177-186.

Boylan, N. and White, D.J. 2013. Depth-averaged numerical modelling of submarine slide run-out in softening soil. *Canadian Geotechnical J.*, under review.

Bransby, M.F. and O'Neill, M.P. 1999. Drag anchor fluke soil interaction in clays. *Proc. 7th Int. Symp. on Numerical Models in Geomechanics*, Graz, 489–494.

Bransby, M.F. and Randolph, M.F. 1998. Combined loading of skirted foundations. *Géotechnique* 48(5), 637-655.

Bransby, M.F. and Randolph, M.F. 1999. The effect of embedment depth on the undrained response of skirted foundations to combined loading. *Soils and Foundations* 39(4), 19-33.

Bransby, M.F. and Yun, G.J. 2009. The undrained capacity of skirted strip foundations under combined loading. *Géotechnique* 59(2), 115-125.

Bretelle, S. and Wallerand, R. 2013. Fondations superficielles glissantes pour l'offshore profond – méthodologie de dimensionnement. *Proc. 18th Int. Conf. on Soil Mechanics and Geotechnical Eng.*, Paris.

Bruton, D.A.S., Carr, M. and White, D.J. 2007. The influence of pipe-soil interaction on lateral buckling and walking of pipelines: the SAFEBUCK JIP. *Proc. 6th Int. Conf. on Offshore Site Investigation and Geotechnics*, London, 133–150.

Bruton, D.A.S., White, D.J., Carr, M. and Cheuk, C.Y. 2008. Pipe-soil interaction during lateral buckling and pipeline walking - the SAFEBUCK JIP. *Proc. Offshore Technology Conf.*, Houston, Paper OTC 19589.

Cassidy, M.J., Gaudin, C., Randolph, M.F., Wong, P.C., Wang, D. and Tian, Y. 2012. A plasticity model to assess the keying of plate anchors. *Géotechnique* 62(9), 825-836.

Cathie, D.N., Jaeck, C., Ballard, J.C. and Wintgens J.F. 2005. Pipeline geotechnics: State of the art. *Proc. Int. Symp. on Frontiers in Offshore Geotechnics, ISFOG*, Perth, 95-114.

Chatterjee, S., Randolph, M.F. and White, D.J. 2012a. The effects of penetration rate and strain softening on the vertical penetration resistance of seabed pipelines. *Géotechnique* 62(7), 573–582.

Chatterjee, S., White, D.J. and Randolph, M.F. 2012b. Numerical simulations of pipe-soil interaction during large lateral movements on clay. *Géotechnique* 62(8), 693–705.

Chatterjee, S., Randolph, M.F. and White, D.J. 2013. A parkable piezoprobe for measuring c_v at shallow depths for offshore design. *Géotechnique*, under review.

Cheuk C.Y. and White D.J. 2011. Modelling the dynamic embedment of seabed pipelines, *Géotechnique* 61(1), 39-57.

Colliat, J.L. and Colliard, D. 2010. Set-up of suction piles in deepwater Gulf of Guinea clays. *Proc. 2nd Int. Symp. on Frontiers in Offshore Geomechanics, ISFOG 2010*, Perth, 723–727.

Colliat, J.-L., Dendani, H., Puech, A. and Nauroy, J.-F. 2010. Gulf of Guinea deepwater sediments: Geotechnical properties, design issues and installation experiences. *Proc. 2nd Int. Symp. on Frontiers in Offshore Geotechnics*, *ISFOG 2010*, Perth, 59-86.

DeJong, J. and Randolph, M.F. 2012. Influence of partial consolidation during cone penetration on estimated soil behavior type and pore pressure dissipation measurements. *J. Geotech. Geoenviron. Eng.,* ASCE, 138(7), 777–788.

DeJong, J. et al. (34 authors) 2013. Biogeochemical processes and geotechnical applications: progress, opportunities and challenges. *Géotechnique* 63(4), 287-301.

DeJong, J.T., White, D.J. and Randolph, M.F. 2006. Microscale evolution of soil-structure interface behaviour during CNS cyclic shearing using PIV. *Soils and Foundations*, 46(1), 15-28.

DeJong, J.T., Yafrate, N.J. and DeGroot, D.J. 2011. Evaluation of undrained shear strength using full flow penetrometers. *J. Geotech. Geoenviron. Eng.*, ASCE, 137(1), 14-26.

DeJong, J.T., Yafrate, N.J. and Randolph, M.F. (2008). Use of pore pressure measurements in a ball full-flow penetrometer. *Proc. 3rd Int. Conf. on Site Characterization*, Taipei, 1269-1275.

Dimmock, P., Clukey, E.C., Randolph, M.F., Gaudin, C. and Murff, J.D. 2013. Hybrid subsea foundations for subsea equipment. *J. Geotech. Geoenviron. Eng.,* ASCE, in press.

Dutt, R. and Ehlers, C. 2009. Set-up of large diameter driven pipe piles in deepwater normally consolidated high plasticity clays. *Proc. Conf. on Offshore Mech. and Arctic Engng.*, *OMAE*, Honolulu, Paper OMAE2009-79012.

Dyson, G.J. and Randolph, M.F. 2001. Monotonic lateral loading of piles in calcareous sand. *J. Geotech. Geoenviron. Eng.,* ASCE, 127(4), 346–352.

Einav, I. and Randolph, M.F. 2005. Combining upper bound and strain path methods for evaluating penetration resistance. *Int. J. Numerical Methods in Engineering* 63(14), 1991-2016.

Einav, I. and Randolph, M.F. 2006. Effect of strain rate on mobilised strength and thickness of curved shear bands. *Géotechnique* 56(7), 501-504.

Elkhatib, S. 2006. *The behaviour of drag-in plate anchors in soft cohesive soils*. PhD Thesis, The University of Western Australia.

Erbrich, C.T., O'Neill, M.P., Clancy, P. and Randolph, M.F. 2010. Keynote Lecture: Axial and lateral pile design in carbonate soils. *Proc. 2nd Int. Symp. on Frontiers in Offshore Geotechnics, ISFOG 2010*, Perth, 125-154.

Fahey, M. and Carter, J.P. 1993. A finite element study of the pressuremeter test in sand using a nonlinear elastic plastic model. *Canadian Geotechnical J.* 30, 348-362.

Feng, X., Randolph, M.F., Gourvenec, S. and Wallerand, R. 2013. Design approach for rectangular mudmats under fully three-dimensional loading. *Géotechnique*, under review.

Finnie, I.M.S. and Morgan, N. 2004. Torsional loading of subsea structures. *Proc. Int. Offshore and Polar Engng Conf.*, Toulon, 326-333.

Gaudin, C., Randolph, M.F., Feng, X., Clukey, E.C. and Dimmock, P. 2012. Centrifuge modelling of a hybrid foundation for subsea equipment. *Proc. 7th Int. Conf. Offshore Site Investigation and Geotechnics*, Soc. for Underwater Technology, London, 411-420.

Gibson, R.E. 1974. The analytical method in soil mechanics. *Géotechnique* 24(2), 115-140.

Gilbert, R.B., Chen, J.-Y., Materek, B., Puskar, F., Verret, S., Carpenter, J., Young, A., and Murff, J.D. 2010. Comparison of observed and predicted performance for jacket pile foundations in hurricanes. *Proc. Offshore Technology Conf.*, Houston, Paper OTC 20861.

Gourvenec, S. 2007a. Shape effects on the capacity of rectangular footings under general loading. *Géotechnique* 57(8), 637-646.

Gourvenec, S. 2007b. Failure envelopes for offshore shallow foundation under general loading. *Géotechnique* 57(9), 715-727.

Gourvenec, S. 2008. Undrained bearing capacity of embedded footings under general loading. *Géotechnique* 58(3), 177–185.

Gourvenec, S. and Barnett, S. 2011. Undrained failure envelope for skirted foundations under general loading. *Géotechnique* 61(3), 263–270.

Gourvenec, S. and Randolph, M.F. 2003. Effect of strength non-homogeneity on the shape and failure envelopes for combined loading of strip and circular foundations on clay. *Géotechnique* 53(6), 575-586.

Guha, I. 2013. *Structural analysis of submarined pipelines under submarine slide and thermal loading*. Forthcoming PhD thesis, University of Western Australia.

Guo, W.D. and Randolph, M.F. 1997. Vertically loaded piles in non-homogeneous media. *Int. J. Num. and Anal. Methods in Geomechanics* 21(8), 507-532.

Hill, H.J., White, D.J., Bruton, D.A.S., Langford, T., Meyer, V., Jewell, R.A. and Ballard, J.-C. 2012. A new framework for axial pipe-soil resistance illustrated by a range of marine clay datasets. *Proc. 7th Int. Conf. Offshore Site Investigation and Geotechnics*, Soc. for Underwater Technology, London, 367-377.

Hodder, M.S., White, D.J. and Cassidy, M.J. 2013. An effective stress framework for the variation in penetration resistance due to episodes of remoulding and reconsolidation. *Géotechnique* 63(1), 30–43.

Houlsby, G.T. and Puzrin, A.M. 1999. The bearing capacity of a strip footing on clay under combined loading. *Proc. R. Soc. London A* 455, 893–916.

ISO 2003. *ISO 19901-4: Petroleum and natural gas industries — Specific requirements for offshore structures — Part 4: Geotechnical and foundation design considerations, 1st Edition.* International Standards Organisation, Geneva.

ISO 2007. *ISO 19902: Petroleum and natural gas industries — Fixed steel offshore structures, 1st Edition*. International Standards Organisation, Geneva.

Jardine, R.J., Chow, F.C., Overy, R.F. and Standing, J.R. 2005. *ICP design methods for driven piles in sands and clays*. Telford, London.

Jeanjean, P. 2006. Set-up characteristics of suction anchors for soft Gulf of Mexico clays: experience from field installation and retrieval. *Proc. Offshore Technology Conf.*, Houston, Paper OTC 18005.

Jeanjean, P. 2009. Re-assessment of p-y curves for soft clays from centrifuge testing and finite element modeling. *Proc. Offshore Technology Conf.*, Houston, Paper OTC 20158.

Jeanjean, P. 2012. State of practice: Offshore geotechnics throughout the life of an oil and gas field. *Proc. GeoCongress 2012, State of the Art and Practice in Geotechnical Engineering*, Oakland, Ca, ASCE Geotechnical Special Publication No. 226, 643-677.

Jeanjean, P., Watson, P.G., Kolk, H. and Lacasse, S. 2010. RP 2GEO: The new API recommended practice for geotechnical engineering. *Proc. Offshore Technology Conf.*, Houston, Paper OTC 20631.

Kelleher, P.J. and Randolph, M.F. 2005. Seabed geotechnical characterisation with the portable remotely operated drill. *Proc. Int. Symp. on Frontiers in Offshore Geotechnics, ISFOG*, Perth, 365-371.

Klar, A. and Pinkert, M.F. 2010. Steady-state solution for cylindrical penetrometers. *Int. J. Num. and Anal. Methods in Geomechanics* 34, 645-659.

Klar, A. and Randolph, M.F. 2008. Upper bound and load displacement solutions for laterally loaded piles in clay based on energy minimisation. *Géotechnique* 58(10), 815-820.

Kraft, L.M., Ray, R.P. and Kagawa, T. 1981. Theoretical t-z curves. *J. Geot. Eng. Div., ASCE*, 107(11), 1543-1561.

Kuo, M.Y-H. and Bolton, M.D. 2013. The nature and origin of deep ocean clay crust from the Gulf of Guinea. *Géotechnique* in press.

Lehane, B.M., Schneider, J.A. and Xu, X.2005. The UWA-05 method for prediction of axial capacity of driven piles in sand. *Proc. Int. Symp. on Frontiers in Offshore Geomechanics ISFOG*, Perth, 683–689.

Lenci, S. and Callegari, M. 2005. Simple analytical models for the J-lay problem, *Acta Mechanica* 178, 23-39.

Low, H.E., Landon, M.M., Randolph, M.F. and DeGroot, D.J. 2011. Geotechnical characterisation and engineering properties of Burswood clay. *Géotechnique* 61(7), 575-591.

Low, H.E., Lunne, T., Andersen, K.H., Sjursen, M.A., Li, X. and Randolph, M.F. 2010. Estimation of intact and remoulded undrained shear strength from penetration tests in soft clays. *Géotechnique* 60(11), 843-859.

Low, H..E., Randolph, M.F. and Kelleher, P. 2007. Estimation of in-situ coefficient of consolidation from dissipation tests with different penetrometers. *Proc. 6th Int. Conf. Offshore Site Investigation and Geotechnics*, Soc. for Underwater Technology, London, 547-556.

Mahmoodzadeh, H. and Randolph, M.F. 2013. The effect of partial consolidation on the subsequent dissipation test. Under review.

Mahmoodzadeh, H., Wang, D. and Randolph, M.F. 2013. Interpretation of piezoball dissipation test in kaolin clay. Under review.

Martin, C.M. 2001. Vertical bearing capacity of skirted circular foundations on Tresca soil. *Proc. 15th Int. Conf. on Soil Mechanics and Geotechnical Engineering*, Istanbul, 1, 743-746.

Martin, C.M. and Randolph, M.F. 2006. Upper bound analysis of lateral pile capacity in cohesive soil. *Géotechnique* 56(2), 141-145.

Martin, C.M. and White, D.J. 2012. Limit analysis of the undrained bearing capacity of offshore pipelines. *Géotechnique* 62(9), 847-863.

Merifield, R.S., White, D.J. and Randolph, M.F. 2008. The ultimate undrained resistance of partially-embedded pipelines. *Géotechnique* 58(6), 461-470.

Merifield, R.S., White, D.J. and Randolph, M.F. 2009. The effect of surface heave on the response of partially-embedded pipelines on clay. *J. Geotech. Geoenviron. Eng.*, ASCE, 135(6), 819-829

Murff, J.D. 1975. Response of axially loaded piles. *J. Geot. Eng. Div., ASCE* 101(GT3), 356-360.

Murff, J.D. 1980. Pile capacity in a softening soil. *Int. J. Numerical and Analytical Methods in Geomechanics* 4, 185–189.

Murff, J.D. 1994. Limit analysis of multi-footing foundation systems. *Proc. 8th Int. Conf. on Computer Methods and Advances in Geomechanics*, Morgantown, 1, 223-244.

Murff, J.D. 2012. Inaugural McClelland lecture: Estimating the capacity of offshore foundations. *Proc. 7th Int. Conf. Offshore Site Investigation and Geotechnics*, Soc. for Underwater Technology, London, 9-44.

Murff, J.D., Aubeny, C.P. and Yang, M. 2010. The effect of torsion on the sliding resistance of rectangular foundations. *Proc, 2nd Int. Symp. Frontiers in Offshore Geotechnics, ISFOG 2010*, Perth, 439-443.

Murff, J.D. and Hamilton, J.M. 1993. P-ultimate for undrained analysis of laterally loaded piles. *J. Geot. Eng. Div., ASCE*, 119(1), 91-107.

Mylonakis, G. and Gazetas, G. 1998. Settlement and additional internal forces of grouped piles in layered soil. *Géotechnique* 48(1), 55–72.

Neubecker, S.R. and Randolph, M.F. 1995. Profile and frictional capacity of embedded anchor chain. *J. Geot. Eng. Div., ASCE*, 121(11), 787-803.

Neubecker S.R. and Randolph M.F. 1996. The performance of drag anchors and chain systems in cohesive soil. *Marine Georesources and Geotechnology* 14, 77-96.

Novello, E.A. 1999. From static to cyclic p-y data in calcareous sediments. *Proc. 2nd Int. Conf. on Engineering for Calcareous Sediments*, Bahrein, 1, 17–24.

O'Neill, M.P., Bransby, M.F. and Randolph, M.F. 2003. Drag anchor fluke-soil interaction in clay. *Canadian Geotechnical J.* 40(1), 78-94.

Palmer A.C. 2008. Touchdown indentation of the seabed. *Applied Ocean Research* 30, 235-238.

Poulos H.G. 1988 Cyclic stability diagram for axially loaded piles. *J. Geotech. Geoenviron. Eng.,* ASCE, 114 (8), 877-895.

Puech, A., Benzaria, O., Thorel, L., Garnier, J., Foray,P., Silva, M. and Jardine, R.J. 2013. Diagrammes de stabilité cyclique de pieux dans les sables. *Proc. 18th Int. Conf. on Soil Mechanics and Geotechnical Engineering*, Paris.

Randolph, M.F. 1983. Design considerations for offshore piles. *Proc. Conf. on Geot. Practice in Offshore Engng*, ASCE, Austin, 422-439.

Randolph M.F. 2000. Effect of strength anisotropy on capacity of foundations. *Proc. John Booker Memorial Symp.*, Sydney, 313-328.

Randolph, M.F. 2003. 43rd Rankine Lecture: Science and empiricism in pile foundation design. *Géotechnique* 53(10), 847-875.

Randolph, M.F., Hefer, P.A., Geise, J.M. and Watson, P.G. 1998. Improved seabed strength profiling using T-bar penetrometer. *Proc Int. Conf. Offshore Site Investigation and Foundation Behaviour*, Society for Underwater Technology, London, 221-235.

Randolph, M.F. and Hope, S. 2004. Effect of cone velocity on cone resistance and excess pore pressures. *Proc. Int. Symp. On Eng. Practice and Performance of Soft Deposits*, Osaka, 147-152.

Randolph, M.F. and Houlsby, G.T. 1984. The limiting pressure on a circular pile loaded laterally in cohesive soil. *Géotechnique* 34(4), 613-623

Randolph, M.F., Low, H.E. and Zhou, H. 2007. In situ testing for design of pipeline and anchoring systems, *Proc. 6th Int. Conf. on Offshore Site Investigation and Geotechnics*, Soc. for Underwater Technology, London, 251-262.

Randolph, M.F., Martin, C.M. and Hu, Y. 2000. Limiting resistance of a spherical penetrometer in cohesive material. *Géotechnique* 50(5) 573-582.

Randolph, M.F. and Puzrin, A.M. 2003. Upper bound limit analysis of circular foundations on clay under general loading. *Géotechnique* 53(9), 785-796.

Randolph, M.F., Seo, D. and White, D.J. 2010. Parametric solutions for slide impact on pipelines. *J. Geotech. Geoenviron. Eng.*, ASCE, 136(7), 940-949.

Randolph, M.F. and White, D.J. 2008a. Pipeline embedment in deep water: processes and quantitative assessment. *Proc. Offshore Technology Conf.*, Houston, Paper OTC 19128.

Randolph, M.F. and White, D.J. 2008b. Upper bound yield envelopes for pipelines at shallow embedment in clay. *Géotechnique* 58(4), 297-301.

Randolph, M.F. and White, D.J. 2012. Interaction forces between pipelines and submarine slides – a geotechnical viewpoint. *Ocean Engineering* 48, 32-37.

Randolph, M.F., White, D.J. and Yan, Y. 2012. Modelling the axial soil resistance on deep water pipelines. *Géotechnique* 62(9), 837-846.

Randolph, M.F. and Wroth, C.P. 1978. Analysis of deformation of vertically loaded piles. *J. Geot. Eng. Div., ASCE*, 104(GT12), 1465-1488.

Randolph, M.F. and Wroth, C.P. 1979. An analytical solution for the consolidation around a driven pile. *Int. J. Num. and Anal. Methods in Geomechanics* 3(3), 217-229.

Sahdi, F., Gaudin, C., White, D.J., Boylan, N. and Randolph, M.F. 2013. Centrifuge modelling of active slide-pipeline loading in soft clay. *Géotechnique* (under review).

Salgado R, Lyamin A.V., Sloan S.W. and Yu H.S. 2004. Two and three-dimensional bearing capacity of foundations in clay. *Géotechnique* 54(5), 297-306.

Schneider, J. A., Lehane, B. M., and Schnaid, F. 2007. Velocity effects on piezocone tests in normally and overconsolidated clays. *Int. J. Physical Modelling in Geotechnics* 7(2), 23–34.

Schneider, J.A., Xu, X. and Lehane, B.M. 2008. Database assessment of CPT based design methods for axial capacity of driven piles in siliceous sands. *J. Geotech. Geoenviron. Eng.,* ASCE, 134(9), 1227-1244.

Stewart, D.P. and Randolph, M.F. 1994. T-Bar penetration testing in soft clay. *J. Geot. Eng. Div., ASCE* 120(12), 2230-2235.

Suryasentana, S.K. and Lehane, B.M. 2013. Numerical derivation of CPT-based p-y curves for piles in sand. *Géotechnique*, under review.

Taiebat, H.A. and Carter, J.P. 2000. Numerical studies of the bearing capacity of shallow foundations on cohesive soil subjected to combined loading. *Géotechnique* 50(4), 409-418.

Taiebat, H.A. and Carter, J.P. 2002. Bearing capacity of strip and circular foundations on undrained clay subjected to eccentric loads. *Géotechnique* 52(1), 61-64.

Taiebat H.A., and Carter, J.P. 2010. A failure surface for circular footings on cohesive soils. *Géotechnique* 60(4), 265–273.

Teh, C.I. and Houlsby, G.T. 1991. An analytical study of the cone penetration test in clay. *Géotechnique* 41(1), 17–34.

Tian, Y., Cassidy, M.J., Gaudin, C. and Randolph, M.F. 2013. Considerations on the design of keying flap of plate anchors. *J. Geotech. Geoenviron. Eng.*, ASCE, in press.

Wei, Q., Cassidy, M.J., Tian, Y. and Gaudin, C. 2013. Incorporating shank resistance into prediction of the keying behaviour of suction embedded plate anchors. Under review.

Wesselink, B.D., Murff, J.D., Randolph, M.F., Nunez, I.L. and Hyden, A.M. 1988. Analysis of centrifuge model test data from laterally loaded piles in calcareous sand. *Proc. Int. Conf. on Engineering for Calcareous Sediments*, Perth, 1, 261-270.

Westgate, Z.J., Randolph, M.F., White D.J. and Li, S. 2010. The influence of sea state on as-laid pipeline embedment: a case study, *Applied Ocean Research* 32(3), 321-331.

Westgate, Z., White, D.J. and Randolph, M.F. 2012. Field observations of as-laid pipeline embedment in carbonate sediments. *Géotechnique* 62(9), 787-798.

Westgate, Z., White, D.J. and Randolph, M.F. 2013. Modelling the embedment process during offshore pipe laying on fine-grained soils. *Canadian Geotechnical Journal*, in press.

White D.J., Bolton M.D., Ganesan S.A., Bruton D.A.S., Ballard J.-C. and Langford T. (2011). SAFEBUCK JIP: Observations from model testing of axial pipe-soil interaction on soft natural clays. *Proc. Offshore Technology Conf.*, Houston, Paper OTC 21249.

White, D.J. and Cathie, D.N. 2010. Geotechnics for subsea pipelines. *Proc. 2nd Int. Symp. on Frontiers in Offshore Geotechnics, ISFOG 2010*, Perth, 87-123.

White, D.J. and Lehane, B.M. 2004. Friction fatigue on displacement piles in sand. *Géotechnique* 54(10), 645–658.

White, D.J., Schneider, J.A. and Lehane, B.M. 2005. The influence of effective area ratio on shaft friction of displacement piles in sand. *Proc. Int. Symp. on Frontiers in Offshore Geomechanics, ISFOG*, Perth, 741–747.

Yang, M., Aubeny, C.P. and Murff, J.D. 2010. Undrained capacity of plate anchors under general loading. *J. Geotech. Geoenviron. Eng.*, ASCE 136(10), 1383-1393.

Yang, M., Aubeny, C.P. and Murff, J.D. 2012. Behaviour of suction embedded plate anchors during the keying process. *J. Geotech. Geoenviron. Eng.*, ASCE 138(2), 174–183.

Yi, J.T., Goh, S.H., Lee, F.H. and Randolph, M.F. 2012. A numerical study of cone penetration rate effects, *Géotechnique* 62(8),707-719.

Yuan F., Wang L., Guo, Z. and Xie Y.G. 2012. Analytical analysis of pipeline-soil interaction during J-lay on a plastic seabed with bearing resistance proportional to depth. *Applied Ocean Research* 36, 60-68.

Yun, G. and Bransby, M.F. 2007. The undrained vertical bearing capacity of skirted foundations. *Soils and Foundations* 47(3), 493-505.

Yun, G.J., Maconochie, A., Oliphant, J. and Bransby, M.F. 2009. Undrained capacity of surface footings subjected to combined V-H-T loading. *Proc. Int. Offshore and Polar Engineering Conference,* Osaka, Paper 2009-TPC-614.

Zakeri, A. 2009. Submarine debris flow impact on suspended (free-span) pipelines: normal and longitudinal drag forces. *Ocean Engineering* 36(6-7), 489-499.

Zakeri, A., Chi, K. and Hawlader, B. 2011. Centrifuge modeling of glide block and out-runner block impact on submarine pipelines. *Proc. Offshore Technology Conf.*, Houston, Paper OTC 21256.

Zhang, C., White, D.J., Randolph, M.F. 2011. Centrifuge modelling of the cyclic lateral response of a rigid pile in soft clay. *J. Geotech. Geoenviron. Eng.*, ASCE, 137(7), 717-729.

Zhou, H. and Randolph, M.F. 2006. Large deformation analysis of suction caisson installation in clay. *Canadian Geotechnical J.* 43, 1344-1357.

Zhou, H. and Randolph, M.F. 2009a. Resistance of full-flow penetrometers in rate-dependent and strain-softening clay. *Géotechnique* 59(2), 79-86.

Zhou, H. and Randolph, M.F. 2009b. Numerical investigations into cycling of full-flow penetrometers in soft clay. *Géotechnique* 59(10), 801-812.